Petroleum Science 20 (2023) 177–198

Contents lists available at ScienceDirect

Petroleum Science

journal homepage: www.keaipublishing.com/en/journals/petroleum-science

Original Paper

Sensitivity of seismic attenuation and dispersion to dynamic elastic interactions of connected fractures: Quasi-static finite element modeling study

Yan-Xiao He [a, b, c], Wen-Tao He [d], Meng-Fan Zhang [c], Jia-Liang Zhang [e], Wei-Hua Liu [f], Xiao-Yi Ma [f], Gen-Yang Tang [c], Shang-Xu Wang [c, *], Guo-Fa Li [c], Jun-Zhou Liu [a, b, g], Xiang-Long Song [h]

[a] State Key Laboratory of Shale Oil and Gas Enrichment Mechanisms and Effective Development, Beijing, 100083, China
[b] Sinopec Key Laboratory of Seismic Elastic Wave Technology, Beijing, 100083, China
[c] State Key Laboratory of Petroleum Resources and Prospecting, CNPC Key Lab of Geophysical Exploration, China University of Petroleum (Beijing), Beijing, 102249, China
[d] CNOOC (China) Co., Ltd. Hainan Branch, Haikou, Hainan, 570311, China
[e] PetroChina Dagang Oilfield, Tianjin, 300280, China
[f] Sinopec Geophysical Research Institute, Nanjing, Jiangsu, 211103, China
[g] Sinopec Petroleum Exploration and Production Research Institute, Beijing, 100083, China
[h] Chinese Academy of Geological Sciences, Beijing, 100037 China

ARTICLE INFO

Article history:
Received 27 January 2022
Received in revised form
17 April 2022
Accepted 19 August 2022
Available online 26 August 2022

Edited by Jie Hao

Keywords:
Attenuation and dispersion
Rock physics
Fractured media
Frequency dependence
Numerical study

ABSTRACT

Prediction of seismic attenuation and dispersion that are inherently sensitive to hydraulic and elastic properties of the medium of interest in the presence of mesoscopic fractures and pores, is of great interest in the characterization of fractured formations. This has been very difficult, however, considering that stress interactions between fractures and pores, related to their spatial distributions, tend to play a crucial role on affecting overall dynamic elastic properties that are largely unexplored. We thus choose to quantitatively investigate frequency-dependent P-wave characteristics in fractured porous rocks at the scale of a representative sample using a numerical scale-up procedure via performing finite element modelling. Based on 2-D numerical quasi-static experiments, effects of fracture and fluid properties on energy dissipation in response to wave-induced fluid flow at the mesoscopic scale are quantified via solving Biot's equations of consolidation. We show that numerical results are sensitive to some key characteristics of probed synthetic rocks containing unconnected and connected fractures, demonstrating that connectivity, aperture and inclination of fractures as well as fracture infills exhibit strong impacts on the two manifestations of WIFF mechanisms in the connected scenario, and on resulting total wave attenuation and phase velocity. This, in turn, illustrates the importance of these two WIFF mechanisms in fractured rocks and thus, a deeper understanding of them may eventually allow for a better characterization of fracture systems using seismic methods. Moreover, this presented work combines rock physics predictions with seismic numerical simulations in frequency domain to illustrate the sensitivity of seismic signatures on the monitoring of an idealized geologic CO_2 sequestration in fractured reservoirs. The simulation demonstrates that these two WIFF mechanisms can strongly modify seismic records and hence, indicating that incorporating the two energy dissipation mechanisms in the geophysical interpretation can potentially improving the monitoring and surveying of fluid variations in fractured formations.

1. Introduction

Natural fractures, the importance of which has been recognized

* Corresponding author.
E-mail address: wangsx@cup.edu.cn (S.-X. Wang).

https://doi.org/10.1016/j.petsci.2022.08.024

for a long time, particularly for shale and many other unconventional reservoirs embodying low effective permeability (e.g., Gurevich et al., 2009; Galvin and Gurevich, 2015; He et al., 2020), are very common geological features over a wide range of scales (from microscale to continental) in the shallower formations of the Earth's crust and tend to predominantly affect much of their mechanical strength as well as hydraulic properties. This is because fracture networks with their typically small fractions in total volume provide the main transports for the pore fluid flow in such kind of reservoirs, and hence significantly enhancing the effective permeability that critically relies on the hydraulic connectivity of mesoscopic fractures. More accurate identification and description of fracture systems from borehole logging and seismic measurements is, therefore, are crucial tasks in the potential applications spanning multiple domains throughout the engineering, environmental and Earth sciences, including hydrocarbon exploration and depletion, civil engineering, geothermal energy production, as well as nuclear waste disposal and geologic CO_2 sequestration, among many others (e.g., Grab et al., 2017; Wang et al., 2019).

Numerous authors have made considerable efforts, via developing numerous rock physics concepts over recent decades, to describe the underlying links between the hydraulic properties of fluid-saturated fractured rocks and their seismic signatures (e.g., see Müller et al., 2010 for a review). Many such analytical solution, which have been applied to relate phase velocity and wave attenuation (or inverse quality factor) observations with the physical state of pore fluid and permeability in the past (e.g., Chapman et al., 2003; Gurevich et al., 2009; Wenzlau et al., 2010; Kong et al., 2013; Guo et al., 2018; Haggenson et al. 2020; He et al., 2021a), are established in the framework of Biot's theory of poroelasticity via representing the mesoscopic fractures with highly permeable heterogeneities embedded in a stiffer porous media (Biot, 1956a, 1956b). In this respect, the conceptual models often assume elastic matrix, fractures with idealized geometrical properties and ignoring crack or contact areas interactions. Furthermore, the noticeable magnitudes of seismic attenuation in a fractured porous reservoir have been recognized to be primarily governed by wave-induced fluid pressure diffusion (WIFPD), also referred to as wave-induced fluid flow (WIFF) between the pore space of the embedding background and fractures, at mesoscopic scales. Especially, a propagating wave caused significant fluid pressure gradients between such domains tend to equilibrate through pressure diffusion process tightly related to hydraulic properties of the fractured rock, and eventually produce strong energy dissipation due to viscous friction, which in turn were magnified in terms of seismic attenuation and velocity dispersion. In addition, there has been increasing evidence, based on laboratory experiments and theoretical works, to imply that the presence of fractures in fluid-saturated media plays a vital role on affecting wave energy dissipation and velocity dispersion, as well as on the effective anisotropy and scattering (e.g., Chapman et al., 2003; Maultzsch et al., 2003; Kong et al., 2013; He et al., 2021b). It is well known that connectivity and aperture of fractures have a significant impact on the overall mechanical fracture properties. Until up now, however, these influences regarding to the seismic attenuation and velocity dispersion measurements in fractured rocks were not exhaustively evaluated, partially owning to the inherent shortcomings in typically existing effective medium theories (e.g., Chapman et al., 2003; Galvin and Gurevich, 2015; Pang et al., 2021) as well the computational costs.

In this sense, numerical modelling schemes implemented recently consisting of commonly solving Biot's (Biot, 1941, 1956a, 1956b) poroelastic equations have become popular and are more flexible to compute seismic attenuation and velocities due to fluid pressure diffusion effects in fluid-saturated heterogeneous rocks over a broad frequency range (e.g., Masson and Pride, 2007; Rubino et al., 2009; Quintal et al., 2011; Tisato and Quintal, 2013; Solazzi et al., 2017; Zheng et al., 2018; Lissa et al., 2019). In such studies, Zhao et al. (2016) and Cao et al. (2019), based on the numerical finite-element modelling, have explored the influences of elastic interactions between pores and cracks on stress field distribution and, consequently, on the overall effective elastic properties in rock samples containing mesoscale fractures of different shapes and orientations. Their results indicate that spatial arrangements of cracks may be reflected in the characteristics of seismic elastic and anisotropy. Using numerical oscillatory compressibility tests, Rubino et al. (2014) have demonstrated the important role played by the geometrical and mechanical details of fracture contact area on seismic attenuation and phase velocity, which may exhibit a distinct dependence on the effective stress state.

Moreover, several authors have demonstrated in their presented studies that wave attenuation and dispersion of phase velocity might embody valuable information about fracture connectivity (e.g., see Rubino et al., 2013b; Quintal et al., 2014; Rubino et al., 2013a). Through three oscillatory relaxation experiments on 2-D synthetic sample based on a numerical solution of Biot's poroelastic consolidation equations (Biot, 1941), Rubino et al. (2016) studied anisotropic WIFF effects and analyzed the associated seismic responses of fluid-saturated porous rocks containing different sets of intersecting fractures. Under the assumption that the total stress equilibrium and Darcy's law are fulfilled simultaneously, their methodology is performed in the space-frequency domain. However, WIFPD effects on seismic signatures of fractures with more realistic connectivity, aperture and inclination of the fractures, as well as the fracture infills, were not considered in these works.

In a fractured fluid-saturated porous rock, WIFPD influences are expressed in two fundamental patterns (e.g., Müller et al., 2010; Rubino et al., 2013a; Rubino et al., 2014; Caspari et al., 2019), including wave-induced fluid flow between fractures (or briefly FF-WIFF) and WIFF between fractures and the embedding host matrix (or briefly FB-WIFF). Correspondingly, strong energy dissipation associated with FF-WIFF exists only within fractures with the characteristic time scale relying on the hydraulic diffusivity of the fractures and the host rock, while FB-WIFF takes place in the host matrix. Thus, a better understanding of the interplay between these two mechanisms provides an essential step towards the accurate estimation of fracture features using seismic methods. And thus in this work, to further explore the implications of seismic attenuation and velocity dispersion phenomena, we seek to extend an numerical approach similar to the one of Quintal et al. (2011) to porous fluid-saturated media containing fractures at the mesoscopic scale and follow the analysis of Rubino et al. (2014) applied to a fracture with varying connectivity. As in Quintal et al. (2011), our study is based on quasi-static finite-element simulations of Biot's poroelastic equations for a linear consolidation process (Biot, 1941) in the space-time domain. The principle goal of this study is to understand in more details these two WIFF-based attenuation mechanisms via a comprehensive analysis of the effects of various fracture properties and the filled fluids on seismic attenuation and phase velocity utilizing a complementary numerical upscale-up technique and thus hopefully, to shed a light on the estimation of frequency-dependent elastic moduli of realistic fracture networks as well as on discrimination of the pressure diffusion associated energy dissipation mechanisms.

This paper is structured as follows. We first introduced the quasi-static numerical scale-up procedure, which is applied for 2-D fractured rock models throughout this study and allows to quality the associated seismic attenuation in responses to WIFF. Thereafter, we describe the matrix and fluid properties of the fractured porous rocks and then proceed to explore the roles played by several key

properties of the media considered on wave attenuation and phase velocity over a broad frequency range. Finally, to explore the importance of these two energy dissipation mechanisms, we also examine reservoir-scale seismic signature changes through incorporating the seimoacoustic results predicted into a geological model and simulating the propagation of seismic waves in a fractured reservoir of geologic CO_2 sequestration.

2. Methodological background

One important idea behind rock physics analysis of seismic wave propagations in Earth's crustal rocks is to enable predication of the effects of attenuation and dispersion related to WIFFs in the presence of mesoscopic fractures and pores, and this has been challenging. Since the stress interactions of fractures tend to produce great impact on dynamic elastic properties which are largely unexplored, we choose to investigate numerically their frequency-dependent characteristics for fractured porous rocks at the scale of a representative sample. Thus, the 2-D numerical quasi-static creep experiments, as proposed by Masson and Pride (2007) based on the poroelastic Biot's equations and later modified by Quintal et al. (2011) using the finite element numerical strategy, and their corresponding isotropic upscaling procedure are employed to calculate the effective seismic properties due to WIFF between fractures and the embedding matrix as well as within connected fractures.

2.1. Biot's consolidation equations

We perform numerical modeling of the quasi-static poroelastic experiment based on the Biot's (1941) consolidation equations instead of Biot's (1956a, 1956b) equations of dynamic poroelasticity. The reason behind this is that the WIFF is dominated by fluid pressure gradients and hence, neglecting the inertial effects can in turn lead to a more efficient strategy to predict and interpret the corresponding seismic acoustic signatures. The associated displacement-pressure formulations of quasi-static poroelasticity of Biot's consolidation equations are presented in Appendix A.

Since the methodology is based on the Biot's (1941) quasi-static poroelastic approximation, it is applicable when the largest frequency considered is significantly smaller than the Biot's critical frequency, at which inertial and viscous forces play equal roles on the pore fluid (e.g., Caspari et al., 2016)

$$f_{\text{Biot}} = \frac{\varphi\eta}{2\pi\kappa\rho_{\text{f}}}, \tag{1}$$

with ρ_{f} denoting the density of the pore fluid, η the fluid viscosity, φ the rock porosity and κ the permeability.

Applying a normal compressive stress in the time domain on the top boundary of a synthetic poroelastic model and setting the bottom displacement to zero, while the lateral boundaries are fixed and no shear stresses are applied to the sample. And thus, we simulate the 2-D pure compression experiment and compute the time-varying strain response and explore the corresponding effects on the pore pressure. Fig. 1 gives a representation of such an experiment. In addition, the stress function, $S(t)$, has been employed to guarantee a broad frequency range within a small time duration

$$S(t) = \frac{S_0}{2}\{1 + \tanh[r(t - t_0)]\}, \tag{2}$$

where S_0 represents the constant amplitude of stress level. The stretching coefficient r is chosen to offer the largest frequency and,

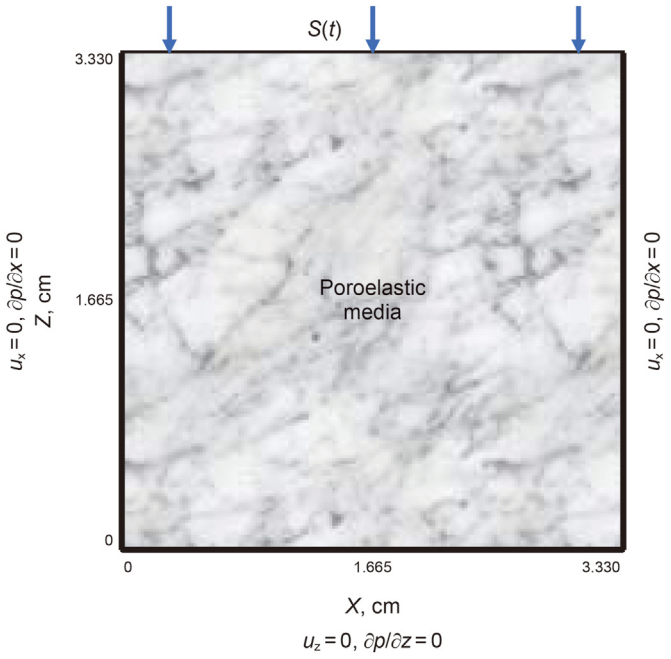

Fig. 1. Schematic representation of a 2-D quasi-static creep compression test applied to a representative elementary volume (REV) of the fluid-saturated poroelastic media. The corresponding boundary conditions indicate that a compressive total force $S(t)$ is applied perpendicularly on the top boundary of the sample, and no fluid flow is allowed for the natural boundary conditions of Biot's equations of consolidation (Biot, 1941) that are essentially in agreement with an undrained rock sample. In addition, the displacements on the bottom boundary and on the lateral boundaries of the sample are set to zero. Elastic moduli of the poroelastic sample are yielded by measuring the resulting strain responses.

the parameter t_0 is amply large that $rt_0 \gg 1$ such that $S(t = 0) \cong 0$. The applied time-varying stress on the top surface of the numerical sample produces fluid pressure differences due to flowing arising within fractures and fractures and the pore space of the background matrix, resulting in significant wave energy dissipation due to viscous dissipation.

2.2. Numerical upscaling procedure

In this study, we investigate the fluid pressure gradients in the mesoscopic scale range, indicating that the characteristic length scale of the fracture L_{frac} are much larger than the typical pore or grain size L_{pore}, but several orders of magnitude smaller than the dominant seismic wavelength λ. Since no fluid flow occurs at the macroscopic scale, the upscaling of Biot's equations of quasi-static poroelasticity allows for spatial and temporal upscaling, generating a homogenous equivalent medium with time- and frequency-dependent effective seismic properties of the fractured porous media. The workflow adopted in this study for the numerical scale-up simulation scheme of seismic attenuation and velocity dispersion corresponding to a vertically propagating compressional wave in fractured poroelastic media is demonstrated in Fig. 2. All the numerical results illustrated here have been yielded through the following procedures:

(1) On a 2-D unstructured triangular finite element mesh allowing the solving of complicated geometries (see Appendix B), a partially fluid saturated numerical rock sample can be represented by a synthetic poroelastic model (i.e., the REV) with the materials to be explored, while the fractured regions fully saturated by another fluid (see Fig. 3).

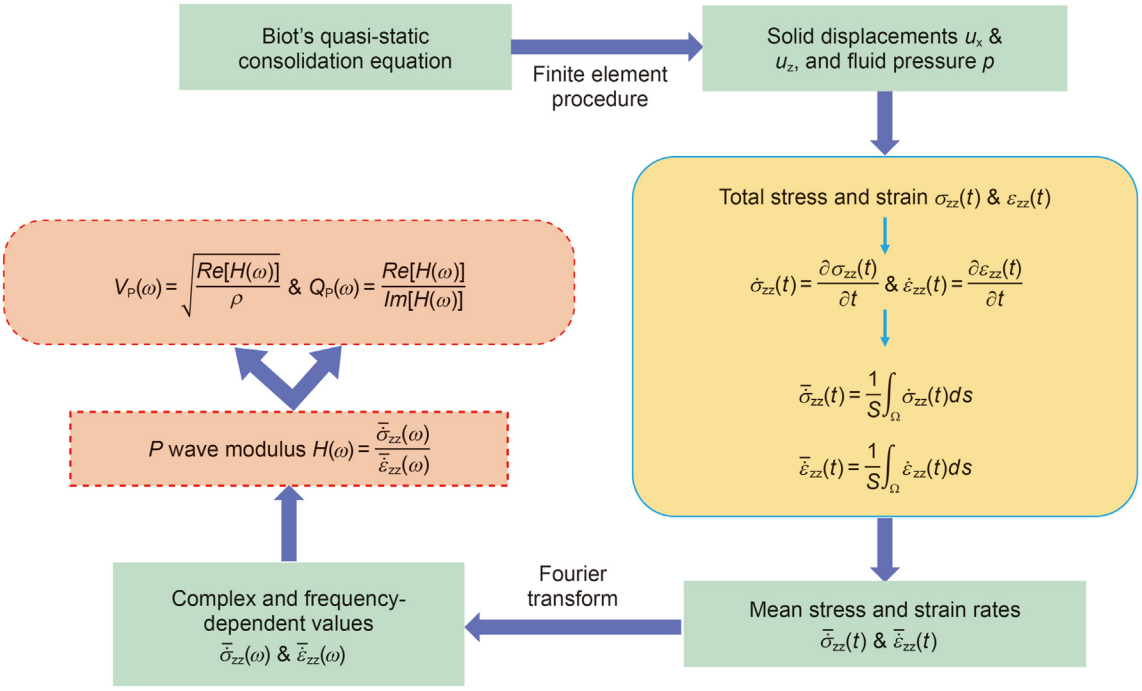

Fig. 2. Workflow for finite element modelling strategy of seismic attenuation $Q_P^{-1}(\omega)$ and velocity dispersion $V_P(\omega)$ of compressional wave in fractured fluid-saturated poroelastic media. Here, the modelling procedure is based on Biot's quasi-static consolidation equations in the solid displacement u and fluid pressure p in the 2-D case (Biot, 1941) rather than Biot (1956a, 1956b) equations of dynamic poroelasticity, since attenuation related to WIFF is dominated by fluid pressure diffusion. A similar procedure of predicting the frequency-dependent $Q_P^{-1}(\omega)$ and $V_P(\omega)$ from the time evolution scheme of the mean normal stress and strain, $\overline{\dot{\sigma}_{zz}}(t)$ and $\overline{\dot{\varepsilon}_{zz}}(t)$, was also presented in Wenzlau et al. (2010).

(2) Via apply normal compressive total forces $S(t)$ in Equation (2) at the top boundary of the square sample, we obtain the total stress $\sigma_{zz}(t)$ and strain $\varepsilon_{zz}(t)$ state throughout the REV at each time step according to solid displacement, u_x and u_z, and fluid pressure p. Especially, variable time steps, with very small time steps at the beginning to accurately resolve complex moduli at high frequencies and larger time steps approaching the end to ensure accuracy at low frequencies, were employed in the 2-D compression simulations.

(3) The stress and strain rates, $\dot{\sigma}_{zz}(t)$ and $\dot{\varepsilon}_{zz}(t)$, which are estimated via taking their time derivatives of σ_{zz} and ε_{zz}, are employed to obtain the time evolution of the mean normal stress and strain rates, $\overline{\dot{\sigma}_{zz}}$ and $\overline{\dot{\varepsilon}_{zz}}$, over the sample domain at the end of the numerical simulation.

(4) Applying a fast Fourier transform algorithm to the mean stress and strain rates, we obtain $\overline{\dot{\sigma}_{zz}}(\omega)$ and $\overline{\dot{\varepsilon}_{zz}}(\omega)$, which are subsequently used to calculate the macroscopic complex-valued and frequency-dependent undrained compressional wave modulus $H(\omega)$ via the expression

$$H(\omega)=\overline{\dot{\sigma}_{zz}}(\omega)\,/\,\overline{\dot{\varepsilon}_{zz}}(\omega), \tag{3}$$

with ω being the angular frequency (rad/s). The corresponding frequency-dependent phase velocity and inverse quality factor associated with a pure undrained compression can be obtained from $H(\omega)$ as

$$V_P(\omega)=\sqrt{\frac{Re(H(\omega))}{\rho}}, \tag{4}$$

$$\frac{1}{Q_P(\omega)}=\frac{Im(H(\omega))}{Re(H(\omega))}, \tag{5}$$

where ρ is the bulk density of fractured fluid-saturated poroelastic medium.

3. Numerical simulations and results

In this section, we seek to complement and extent the initial research efforts of WIFF effects in fractured reservoirs through the use of quasi-static numerical creep experiment, based on the quasi-static poroelasticity equation (Biot, 1941). Since we focus on the undrained seismic acoustic responses, the natural boundary conditions for no fluid flow into the sample or out of it are employed. In order to calculate the stress interaction and the associated effective elastic tensors of the fractured porous rocks, numerical simulation experiments are performed in the time domain with the finite element solver, COMSOL Multiphysics, for poroelastic rheology to a REV of the 2-D heterogeneous medium of interest (Figs. 1 and 3). It is also important to remark that the applied mesh grid is sufficiently small to suitably describe pore pressure diffusion processes related to FF-WIFF and FB-WIFF.

3.1. Matrix parameterization and fluid properties

We model a 2-D poroelastic sample with a square of side length 3.33 cm, corresponding to a homogeneous fluid-saturated sandstone permeated by a set of mesoscopic fractures. The frame of the numerical rock sample consists of quartz grains with the petrophysical properties presented in Table 1. The porous background region corresponds to a moderately stiff sandstone with a porosity of 0.1, while the embedded fracture corresponds to a poorly consolidated sandstone with a porosity of 0.5. The permeability of the numerical rock, κ, is calculated for porosity, φ, according to a Kozeny-Carman formulation (e.g., see Mavko et al., 2009)

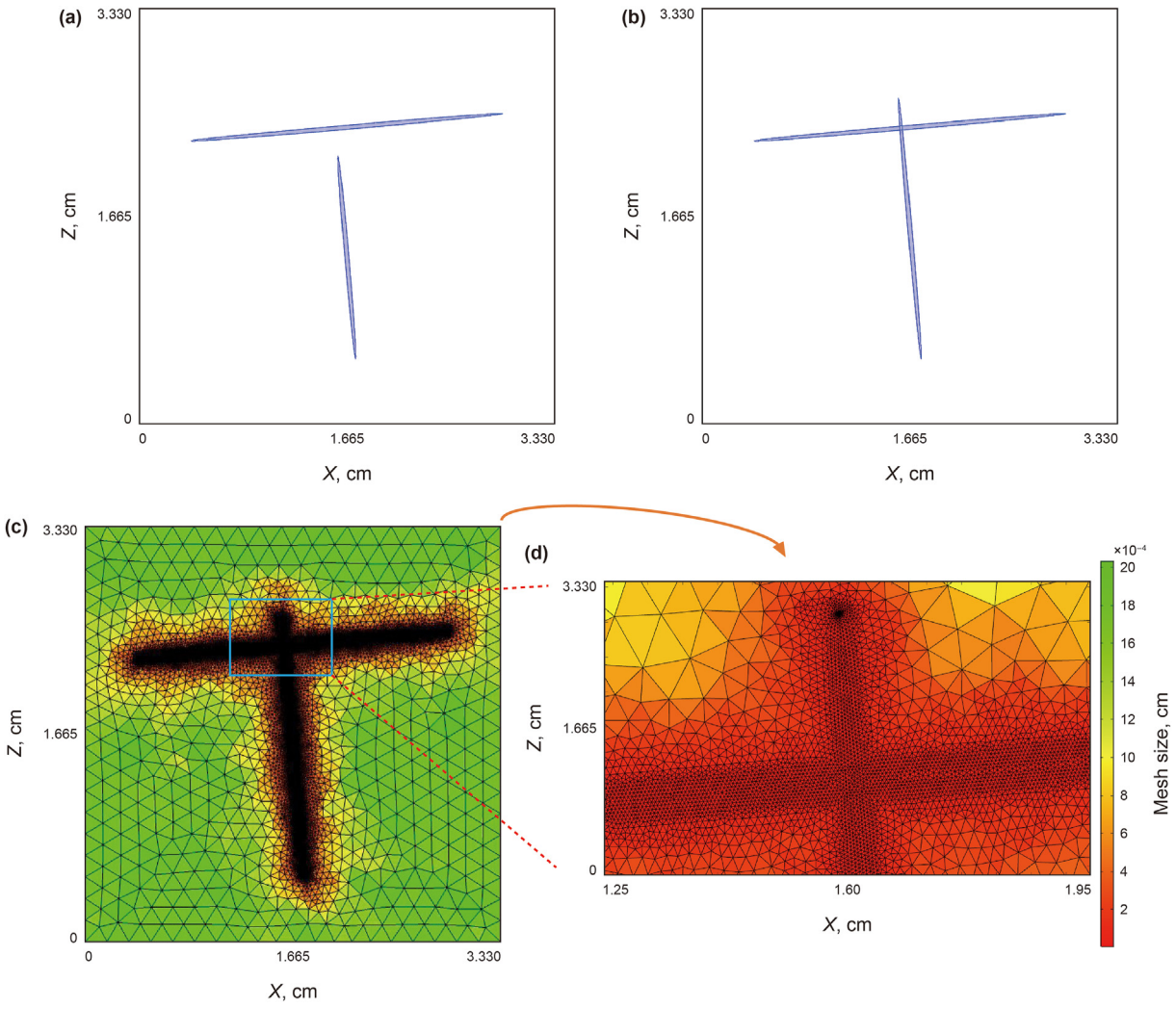

Fig. 3. Synthetic rock samples of connected (a) or unconnected (b) fractures (i.e., Fracture 1 and Fracture 2) designed to investigate the sensitivity of wave attenuation and velocity dispersion to WIFF related to fracture connectivity. Unstructured finite element meshes (c), which have different petrophysical properties and each consists of seven nodal points, are employed to discretize the connected fracture model (a). Blowup of the numerical mesh illustrates that the triangular elements are much smaller in the fractures and their immediate vicinity compared with the regions away from the fractures (d). Moreover, fractures are denoted with hollow elliptical heterogeneities, which are characterized by large porosity and permeability, embedded in the continuous background media of low porosity and permeability.

Table 1
Physical properties of the rock frame for the fractured porous media demonstrated in this study. The parameters were adopted from Rubino et al. (2013b, 2014).

Region	Background	Fracture
Grain bulk modulus, K_s [GPa]	37	37
Grain shear modulus, μ_s [GPa]	44	44
Grain density, ρ_s [g/cm^3]	2.65	2.65
Porosity, φ	0.1	0.5
Permeability, κ [mD]	10^{-2}	10^5
Drained frame bulk modulus, K_d [GPa]	26	0.02
Drained frame shear modulus, K_d [GPa]	31	0.01

$$\kappa = 0.003 * \frac{\varphi^3}{(1-\varphi)^2} d^2, \tag{6}$$

with $d = 1.2 \times 10^{-3}$ cm denoting the averaged grain diameter. In addition, spatial porosity variations imply modifications in other poroelastic properties, like the dry frame moduli. As the poroelastic compressibility contrasts are essential to cause WIFF, it is thus necessary to consider variations in the elastic properties of the dry frame. The dependency of bulk and shear moduli of the dry background on porosity and solid grain properties can be described following the empirical model of Krief et al. (1990).

$$K_d = K_s(1-\varphi)^{3/(1-\varphi)}, \tag{7}$$

$$\mu = K_d \mu_s / K_s, \tag{8}$$

with μ_s representing the shear modulus of the solid grains. In addition, we consider a very low permeability of the background material, $\kappa_b = 10^{-2}$ mD, such as to discriminate the attenuation peak related to FB-WIFF from that corresponding to FF-WIFF. In addition, we consider the porous material composing the fractures a permeability $\kappa_f = 10$ D.

For the following numerical simulations, we employ the poroelastic model containing two quasi-orthogonal mesoscopic fractures with and without intersection (see Fig. 3). We assume that the rock frame properties of the fractures are identical to those of the background material at the grain scale. According to Nakagawa

and Schoenberg (2007), we obtain $K_d^f = 0.02$ GPa and $\mu_d^f = 0.01$ GPa for the drained-frame bulk and shear moduli of the fractures, respectively, through the shear and drained normal compliances

$$\eta_T = \frac{Z}{\mu_d^f}, \tag{9}$$

$$\eta_N = \frac{Z}{\left(K_d^f + 4\mu_d^f/3\right)}, \tag{10}$$

with Z representing the fracture thickness. For the aim of this methodological study, the distinctive contrasts in the material properties are utilized considering the fact that it leads to apparently high attenuation and velocity dispersion associated with WIFF effects. In order to explore how the filled fluid affects the elastic properties of fractured porous reservoirs, the fractures and the background pore spaces are fully saturated with brine, glycerin, oil and CO_2, respectively, for their relatively large range of viscosity. The physical properties of the fluids used are given in Table 2.

3.2. Effects of fracture connectivity on seismic attenuation and velocity dispersion

3.2.1. Sensitivity of attenuation and velocity dispersion to fracture connectivity

Fig. 3 depicts the two synthetic rock samples employed to investigate the fracture connectivity effects on P-wave attenuation and velocity dispersion related to two WIFF mechanisms. The bottom panel of Fig. 3 shows the unstructured finite element mesh with Delaunney triangulation for the numerical simulation algorithm for the synthetic sample containing connected fractures shown in Fig. 3(b). Fig. 4 depicts the snapshots of the 2-D quasi-static creep experiments with brine-saturated fractures and background materials, for the normalized fluid pressure field p at six different times. The snapshots in Fig. 4(a) correspond to a compression test for the P-wave traveling vertically throughout the poroelastic sample containing unconnected fractures (i.e., Fracture 1), while snapshots in Fig. 4(b) correspond to that of the sample embedding connected fractures (i.e., Facture 2). The total stress and strain in normal direction yielded from the numerical experiment are averaged over the sample REV domain. Fig. 4 illustrates the fluid pressure gradients caused by compression as well as the corresponding fluid flow. The results from the simulations shown in Fig. 4(a) and (b) respectively, are illustrated in Fig. 5(a) and (b) for the inverse quality factor, $1/Q_P$, and phase velocity, V_P, of P-wave.

Fig. 5 displays the calculated inverse quality factor and phase velocity for vertically incident P-wave as a function of frequency for the two synthetic samples presented in Fig. 3. The green curve in Fig. 5(a) indicates that the presence of fractures perpendicular to the direction of wave propagation produces significantly marked attenuation with the maximum level within the low seismic frequency band of ~ 2 Hz. Nevertheless, the added non-intersecting fracture parallel to the direction of wave propagation seems to exhibit a moderate to weak influence with respect to the maximum attenuation as addressed in Rubino et al. (2013a). This may be due to the fact that the vertical compressive stress acted on the sample does not strongly alter the fluid pressure within the quasi-vertical fracture and, subsequently, causing no strong WIFF. In addition, the significant compressibility contrast between the quasi-horizontal fracture and the background matrix leads to strong fluid flow between these two regions. It is important to remark that the strong attenuation values due to the FB-WIFF related to the quasi-horizontal fracture (Fig. 5(a)) also correspond to the high velocity dispersion effects over a broad frequency range (Fig. 5(b)), consist with the Kramers-Kronig relationship (e.g., Mavko et al., 2009; Mikhaltsevitch et al., 2016). By comparing the green and red curves, however, we observe significant variations in the overall attenuation characteristics (red curve), as the two quasi-orthogonal mesoscopic fractures intersect. Although the maximum attenuation magnitude decreases apparently, the frequency range in which attenuation occurs broadens. In addition, we find two local attenuation peaks for the synthetic sample under consideration, that is, one peak occurring at a frequency similar to the characteristic frequency of the green curve and corresponding to the fluid flow between fractures and the background matrix, and the remaining one peak at higher frequency of ~ 15000 Hz associated with an additional energy dissipation caused by fluid flow between the connected fractures, i.e., FF-WIFF effects.

It is also interesting to observe in Fig. 4(a) that the posed compressive stress causes a marked fluid pressure perturbation in the highly compliant, quasi-horizontal fracture, compared to the stiffer background rock, and hence leading to significant WIFF across the boundary of the quasi-horizontal fracture and the background matrix. Meanwhile, we note that fluid pressure gradient caused with the quasi-vertical fracture for Fracture 1 (Fig. 3(a)) is relatively low, and thus the presence of this fracture does not substantially alter the overall fluid pressure distribution state. When the two quasi-orthogonal mesoscopic fractures intersect for Fracture 2 (Fig. 3(b)), however, the fluid pressure gradient exhibits a significant alteration, as shown in Fig. 4(b). Note that the quasi-vertical fracture experiences a strong fluid pressure increase before reaching equilibrium, while the fluid pressure field within the quasi-horizontal fracture decreases slightly compared to the un-intersected scenario (Fig. 4(a)). Importantly, the associated fluid pressure gradient alteration is related to the hydraulic connectivity between two quasi-orthogonal fractures and, thus, fluid exchange between the quasi-horizontal fracture and background matrix decreases. We also find that there exists fluid flow between the fracture and background matrix occurring in the vicinity of the quasi-vertical fracture, resulting in the corresponding influence on the attenuation and velocity dispersion behavior for red curve.

Moreover, the results in Figs. 4 and 5 indicate that, at the second attenuation peak with higher frequency, fluid pressure field is

Table 2
Physical properties of fluids used in this study. The parameters were adopted from Quintal et al. (2011) and Yin et al. (2017).

Fluid	Temperature, °C	Bulk modulus, GPa	Viscosity, 10^{-3}Pa•s	Density, g/cm^3
Brine	20	2.28	1.0228	1.013
Oil	20	1.4	20	0.88
Glycerin	20	4.68	1412	1.262
	40	4.36	284	1.249
	60	4.15	81.3	1.235
	80	4.01	31.9	1.221
	100	3.86	14.8	1.208
CO_2 at 50 MPa	40	0.6	0.0117	0.9913

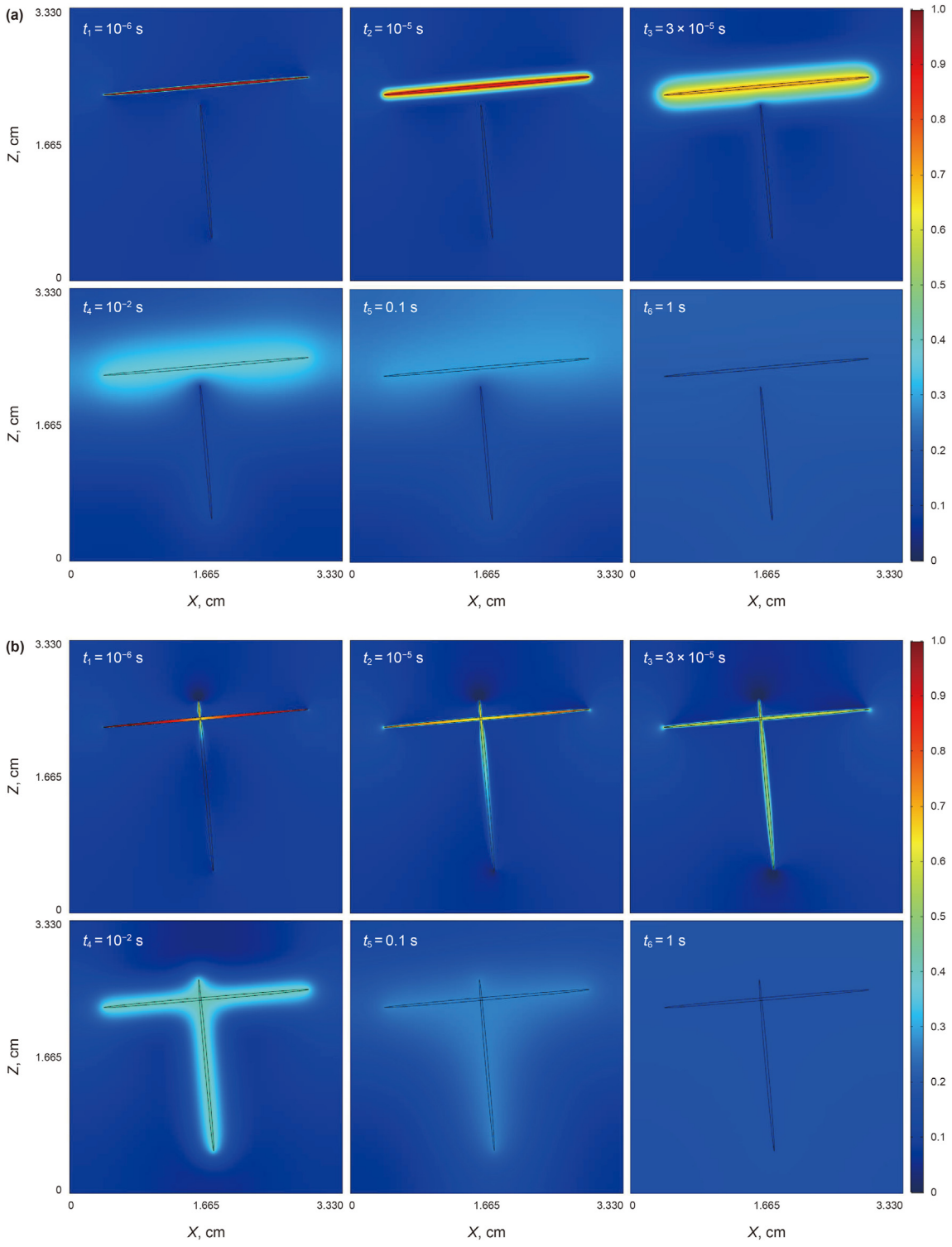

Fig. 4. Snapshots of the normalized fluid pressure field p at times t_1, t_2, t_3, t_4, t_5 and t_6 of the 2-D creep experiments in response to the propagation of a P-wave traveling vertically through the poroelastic samples, where the time evolution of compressive stress $S(t)$ is loaded on the top boundary of the sample. Graph (a) corresponds to the synthetic sample of unconnected fractures (Fracture 1) shown in Fig. 3(a), while Graph (b) corresponds to the synthetic sample of connected fractures (Fracture 2) shown in Fig. 3(b).

much more apparent in the presence of intersected fractures and takes place mainly within the quasi-orthogonal fractures. This makes us more reasonable to account for the corresponding additional attenuation peak as well as velocity dispersion phenomenon. At this higher frequency, there is a strong fluid pressure difference and fluid flow within the quasi-vertical fracture and, correspondingly, fluid is squeezed from the quasi-horizontal fracture due to the fluid pressure increase caused by the vertical compression. It is important to remark that, in Fig. 5(a), although the frequency of second attenuation is well outside the seismic exploration band, the first attenuation peak at lower frequency is also affected by the presence of intersected fractures. Nevertheless,

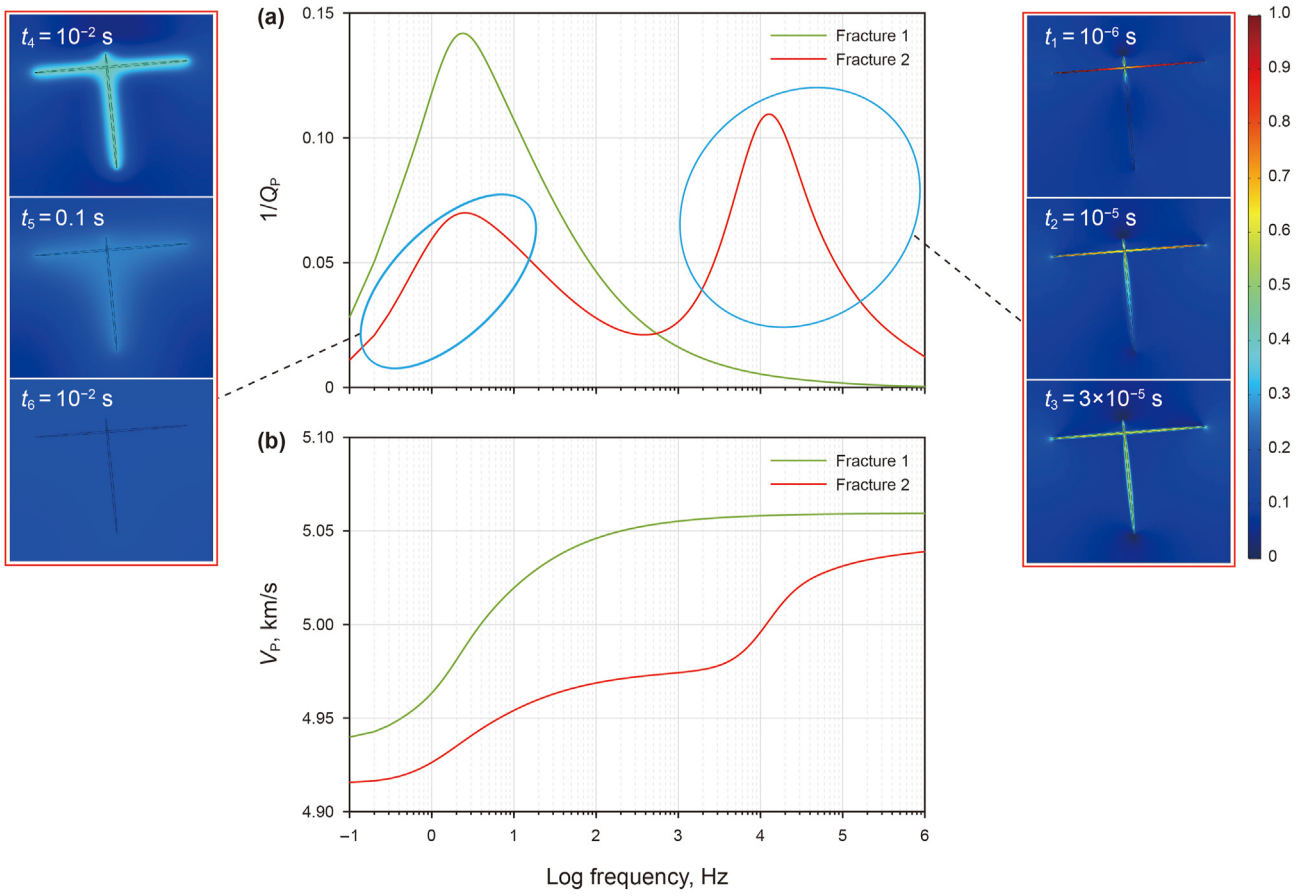

Fig. 5. Numerical results for inverse quality factor $1/Q_P$ (a) and phase velocity V_P (b) of vertically propagating P-wave as functions of frequency, obtained from the 2-D numerical quasi-static creep simulations for the poroelastic rock samples with unconnected fractures (Fracture 1) and connected fractures (Fracture 2) shown in Fig. 3. In graph (a), the two ellipses correspond to the low frequency region where the time increments are amply large to resolve the low-frequency creep process, and the high frequency region where the time increments are small enough to resolve the high-frequency creep process, respectively. The rock-frame and fluid properties are shown in Tables 1 and 2. There are two attenuation peaks, corresponding to two characteristic frequencies of approximately 2 and 15000 Hz that is located outside the frequency band, for the rock sample with two intersected fractures, while a single attenuation peak is found for the rock sample containing two quasi-orthogonal mesoscopic fractures without intersection.

the presence of the quasi-vertical fracture does not alter strongly the fluid pressure distribution in the situation of without intersection. These implications may imply that seismic attenuation and velocity dispersion contain valuable information regard to fracture connectivity. In addition, analysis on the impacts of background porosity on wave attenuation and velocity dispersion is presented in Appendix C.

3.2.2. *WIFF amplification related to fracture intersections*

In order to investigate the dependency between the characteristics of the attenuation peak, as well as the velocity dispersion, associated with fluid flow and the behavior of fractures, we first examine the role played by the addition of quasi-horizontal fracture. Here, two different fractured models, in addition to the samples shown in Fig. 3(a) and (b), for the added quasi-horizontal fractures (Fracture 3 and Fracture 4) are considered while the quasi-vertical fracture remained (Fig. 6). Fig. 7 depicts the inverse quality factor $1/Q_P$ and phase velocity V_P for vertically incident P-wave as a function of frequency for the four synthetic models mentioned. To better understand the results depicted in Fig. 7, we illustrate in Fig. 8 the evolution of fluid pressure field normalized by their maximum values. We observe that the second attenuation peak of higher frequency associated with FF-WIFF exhibits slight discrepancy among the models with interested fractures. This is attributed to the fact that the fluid pressure within the quasi-horizontal fracture arise due to the applied vertical compression. Correspondingly, the produced fluid pressure diffusion inside the quasi-vertical fracture is also marked and hence, leading to larger fluid flow and seismic attenuation. It is also interesting to note that the first attenuation peaks of the fractured models in Fig. 6, at lower frequency related to FB-WIFF, are slightly larger, comparing to that of the model in Fig. 3(b). This is expected, since the significant fluid pressure gradient within the connected fractures results in enhanced fluid flow between fractures and the embedding material and, consequently, higher seismic attenuation. Moreover, for the three models with intersected fractures, for a background permeability of $\kappa^F = 10^{-2}$ mD, the magnitude of seismic attenuation peak controlled by FF-WIFF is slightly larger than that controlled by FB-WIFF.

In this context, it is also interesting to notice that, although the results of three samples with connected fractures show a strong similarity, the addition of quasi-horizontal fractures leads to a decrease in phase velocity V_P (Fig. 7(b)). As well, there are two characteristic frequencies in the intersected models, corresponding to the FB- WIFF and FF-WIFF, respectively. Moreover, we find that the characteristic frequency f_c^F associated with FF-WIFF shifts toward higher frequencies with increasing the addition of the quasi-horizontal fractures and corresponding, the increased fractured permeability κ^F. This is expected, because the characteristic frequency f_c^{FF} of the FF-WIFF attenuation peak is directly proportional

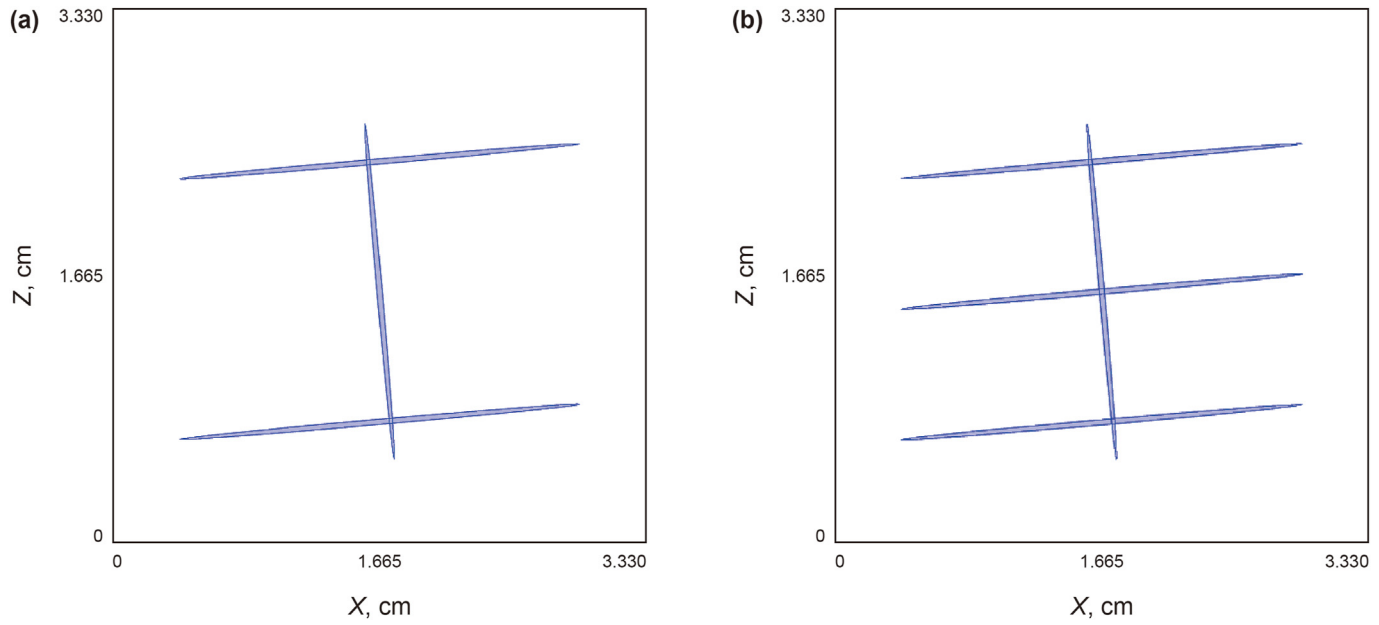

Fig. 6. Illustration of the synthetic rock samples with connected fractures designed to analyze the sensitivity of wave attenuation and velocity dispersion due to WIFF related to fracture connectivity of Fracture 3 (a) and Fracture 4 (b), respectively. The P-wave propagates vertically to the porous sample.

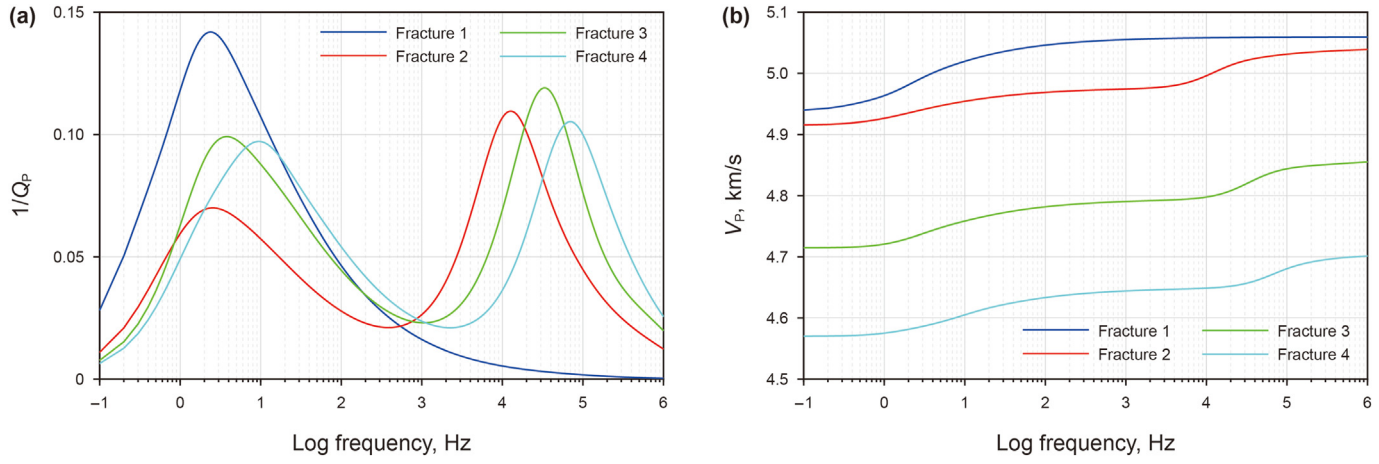

Fig. 7. Numerical results for inverse quality factor $1/Q_P$ (a) and phase velocity V_P (b) of vertically propagating P-wave as functions of frequency, obtained from the 2-D numerical quasi-static creep simulations for the poroelastic rock samples shown in Figs. 3 and 6 considering the unconnected fractures (Fracture 1) and connected fractures (Fracture 2, Fracture 3 and Fracture 4) as denoted in the legend. The rock-frame and fluid properties are shown in Tables 1 and 2. It is important to notice here that two attenuation peaks for the synthetic rock sample with intersected fractures, associated with effects of FB- and FF-WIFF, correspond to two distinct characteristic frequencies.

to the permeability of the fracture material (e.g., see Rubino et al., 2014). We notice that the characteristic frequency of the first attenuation peak f_c^{BF} is also sensitive to the fracture permeability and shifts towards higher frequencies, but remains within the seismic frequency band. This may be related to the strengthened total amount of fluid flow between fractures and the background matrix with adding quasi-horizontal fractures.

From Fig. 4(b) and Fig. 8, we observe that, even though the most significant part of fluid flow seems to happen between the intersected fractures, remarkable fluid flow also happens between fractures and the background regions. This in turn indicates the importance of relative contribution of fluid flow effects on energy dissipation mechanism and thus, various subsegments comprising of the fractures need to be considered so as to better discriminate their respective influences on seismic attenuation and velocity dispersion related to FB- and FF-WIFF.

In order to analyze the role played by the aperture of the fractures, the numerical sample with two interested fractures in Fig. 3(b) are employing via considering various fracture characteristic lengths. Here, we simulate the influence of characteristic lengths of the quasi-horizontal and quasi-vertical fractures, α_1 and α_2, on characteristics of the attenuation peak and the associated velocity dispersion related to FF-WIFF. α_1 and α_2 denote the ratios of the lengths between the major axis and the minor axis for the quasi-horizontal and quasi-vertical fractures, respectively. Fig. 9 depicts the numerical results of inverse quality factor $1/Q_P$ and phase velocity V_P for P-wave as a function of frequency for the fractured sample described above. We see in Fig. 9(a), that although the amplitude of second attenuation peak at higher frequency due to FF-WIFF increases gradually with increasing α_1 and unchanged $\alpha_2 = 50$, the amplitude of first attenuation peak at lower frequency seems unaffected. In addition, the second attenuation peak gets

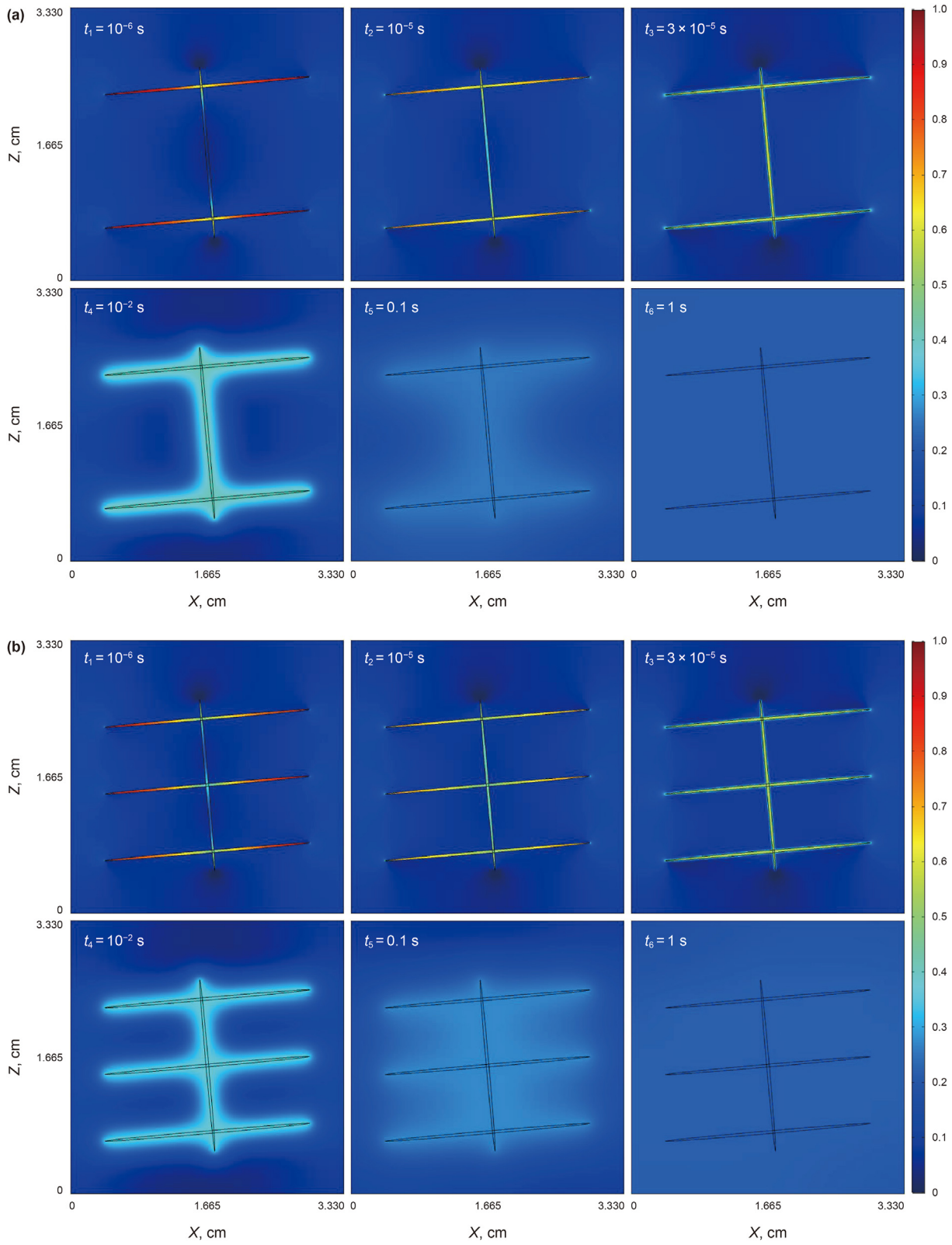

Fig. 8. Snapshots of the normalized fluid pressure field p at times t_1, t_2, t_3, t_4, t_5 and t_6 of the 2-D creep experiments in response to the propagation of a P-wave traveling through the poroelastic samples, where the time evolution of compressive stress $S(t)$ is loaded on the top boundary of the sample. Graph (a) corresponds to the synthetic sample of connected fractures (Fracture 3) shown in Fig. 6(a), while Graph (b) corresponds to the synthetic sample of connected fractures (Fracture 4) shown in Fig. 6(b).

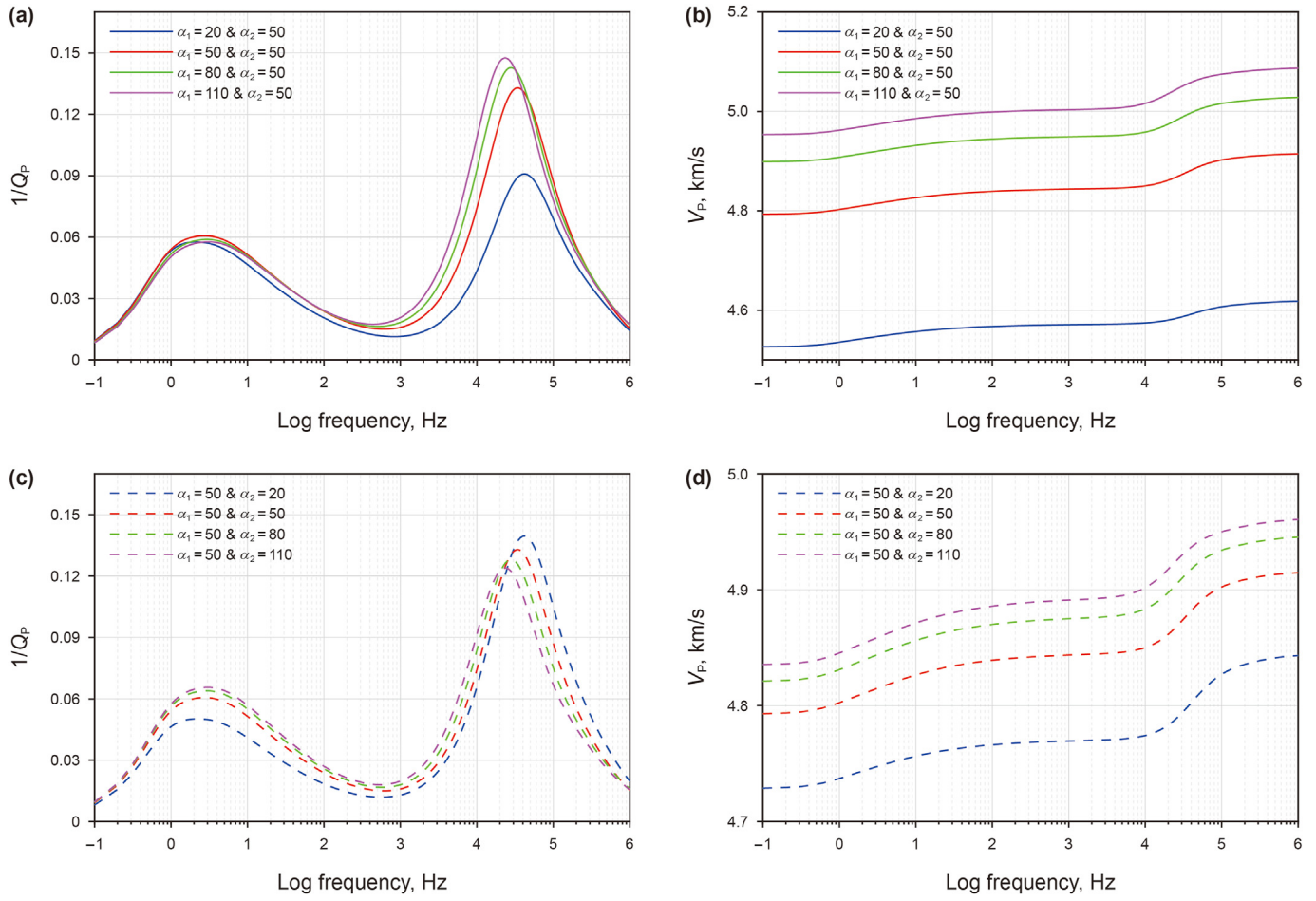

Fig. 9. Numerical results for inverse quality factor $1/Q_P$ (left column) and phase velocity V_P (right column) for vertically propagating P-wave as a function of frequency, obtained for a numerical model consisting of two quasi-orthogonal mesoscopic intersected fractures shown in Fig. 3(b). Colored curves correspond to acoustic responses calculated for the sample with varying fracture characteristic lengths, α_1 and α_2, as indicated in the legend. Here, α_1 and α_2 denote characteristic length of the quasi-horizontal and quasi-vertical fractures, respectively. The rock-frame and fluid properties are shown in Tables 1 and 2

much broader and shifts towards lower frequencies with the increasing α_1, indicating the influence of the characteristic length of the quasi-horizontal fracture α_1 on FB-WIFF and the associated seismic attenuation is, however, rather negligible in this case. Corresponding to the attenuation behavior, we find that phase velocity shows the similar variation characteristics with frequencies, and the velocity increases strongly with the increasing α_1 and the unchanged α_2.

Moreover, we find that for a constant $\alpha_1 = 50$, an increase in the characteristic length of the quasi-vertical fracture α_2 results in a slight increase of the first attenuation peak but a reduction in the level of the second attenuation peak. Interestingly, we also see that the frequency range where the FF-WIFF induced energy dissipation operates shifts towards lower frequencies for increasing characteristic length of the quasi-vertical fracture α_2, or equivalently, decreasing the spacing of the quasi-vertical fractures. However, for FB-WIFF, the characteristic length of the quasi-vertical fracture has no effect on the location of the first attenuation peak. It can also be seen that there are obvious variations in phase velocity dispersion for varying α_2 (see Fig. 9(d)), although the variation is at a less significant level compared to that shown in Fig. 9(b). Hence, the findings of this study also imply that seismic attenuation and the associated velocity dispersion may contain significant information on characteristic lengths of the fractures.

3.3. Role of the intersection angle of fractures on frequency-dependency of seismoacoustic signatures

We also explore the role of the intersection angle between two fractures on attenuation and velocity dispersion, employing a numerical model embodying two fractures of equal length intersecting at their centers for three cases. For the first case, one of the fractures is located horizontally in the center of the rock sample with side length of 3.33 cm and intersected by the other fracture with an angle θ of 30^o, 60^o and 90^o, as shown in Fig. 10. For the second case, two fractures in Fig. 11 are exactly symmetrical with respect to the horizontal plane and in this study, intersection angles θ of 0^o, 30^o, 60^o, 90^o, 120^o, and 150^o are considered. In addition, Fig. 12 illustrates the synthetic rock samples with perpendicularly intersected fractures designed to analyze the role of P-wave propagating direction on wave attenuation and velocity dispersion. A series of intersection angle β of 0^o, 15^o, 30^o, 45^o, 60^o and 75^o, between the vertical axis and one of the fractures, are considered. The corresponding inverse quality factor and phase velocity as a function of frequency are displayed in Fig. 13.

We see from Fig. 13(a) that, while the intersection angle does not affect apparently the characteristic frequency of the two attenuation peaks, their magnitudes are varied significantly. In particular, the value of the first attenuation peak is smallest for $\theta = 90^o$ and gets higher as θ decreases. Conversely, we observe that the

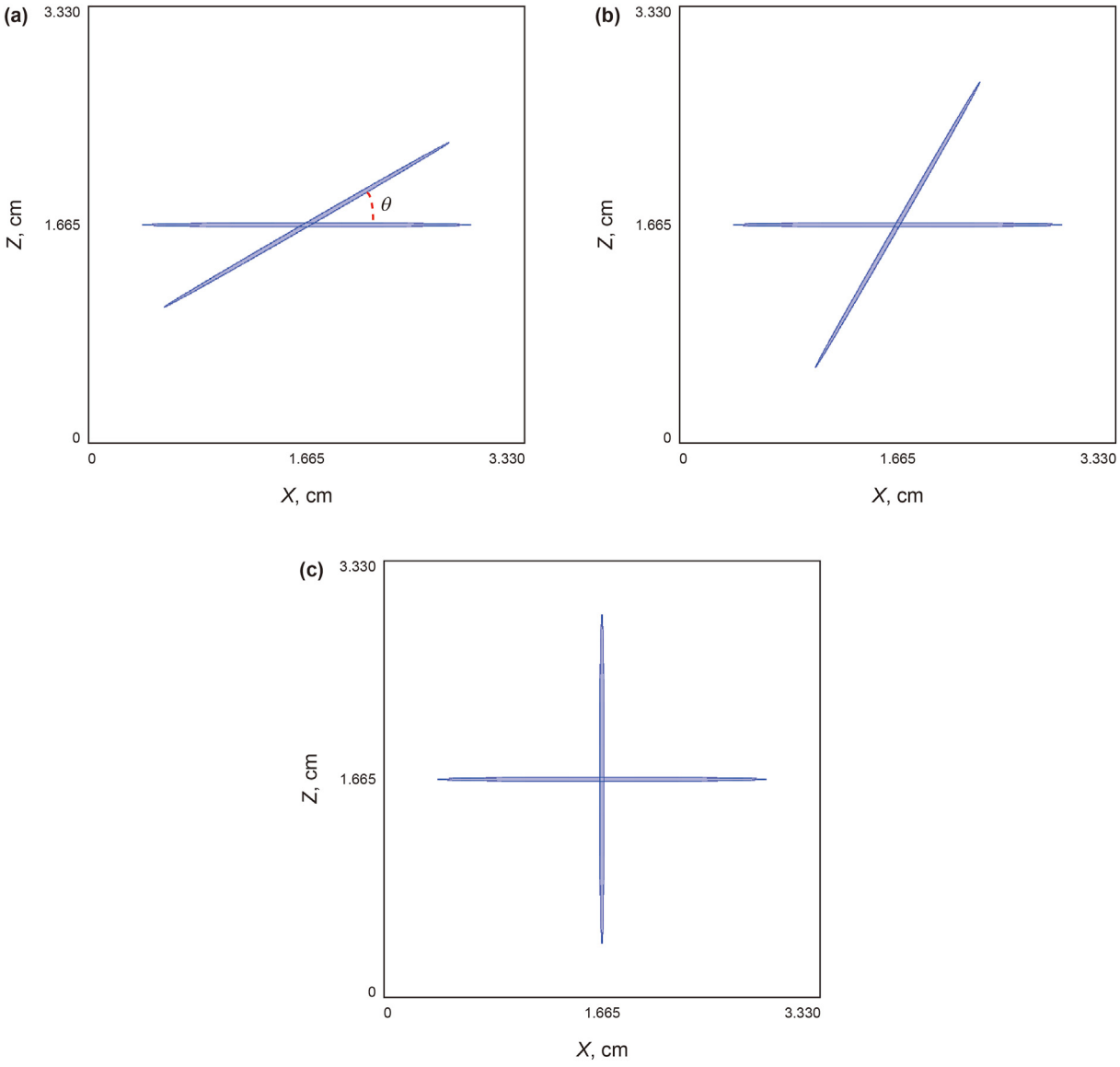

Fig. 10. Illustration of the synthetic rock samples with intersected fractures designed to analyze the role of intersection angle θ between two fractures on attenuation and velocity dispersion, corresponding to $\theta = 30^o$ (a), $\theta = 60^o$ (b), and $\theta = 90^o$ (c), respectively.

amplitude of the second peak is largest for $\theta = 90^o$ and becomes smaller as θ decreases. This corresponds to the phenomenon that the vertical compression acted at the top boundary of the poroelstic sample causes an increase of its fluid pressure as the nonhorizontal fracture becomes more plat and hence, the less amount of fluid is injected from the horizontal fracture. This, in turn, results in the amount of fluid flow inside the fracture system gets less important, while the fluid pressure differences between the fractures and the background regions become increased. Thus, the magnitudes of the attenuation associated with the second peak reduces while the values of the first attenuation peak increases as the nonhorizontal fracture approaches a flat position. The phase velocities in Fig. 13(b) exhibit a similar behavior to seismic attenuation, as the magnitude of velocity dispersion related to FB-WIFF is lowest for $\theta = 90^o$ and gets smaller as θ decreases. As well, the level of velocity dispersion caused by FF-WIFF is highest for $\theta = 90^o$ and reduces as θ decrease.

Fig. 13(c) depicts the inverse quality factor as a function of frequency, corresponding to the fractured rock sample in Fig. 11. It is interesting to note that the intersection angle does not affect strongly the magnitude of the second attenuation, as well as the characteristic frequency of the two attenuation peaks, but produces strong amplitude variations in the attenuation related to FB-WIFF. We find that the level of the first attenuation peak is highest for $\theta = 0^o$ and decreases as θ increases. This is expected, because as the two non-vertical horizontal fractures get more vertical, their fluid pressure decreases. And thus, the fluid pressure gradient between the fractures and the background matrix decreases, whereas the contribution of the amount of fluid flow inside the fracture system to the total attenuation is rather negligible in this case considering the exact symmetry of two fractures with respect to the horizontal plane. The corresponding results are physically meaningful for the phase velocities in Fig. 13(d), as obvious velocity dispersion also occurs at the characteristic transition frequency related to FB-WIFF. As well, we see that phase velocity is sensitive to the intersection angle variations.

It is also interesting to notice that the intersection angle β between the vertical axis and one of the perpendicularly intersected fractures does not influence the location of the two attenuation

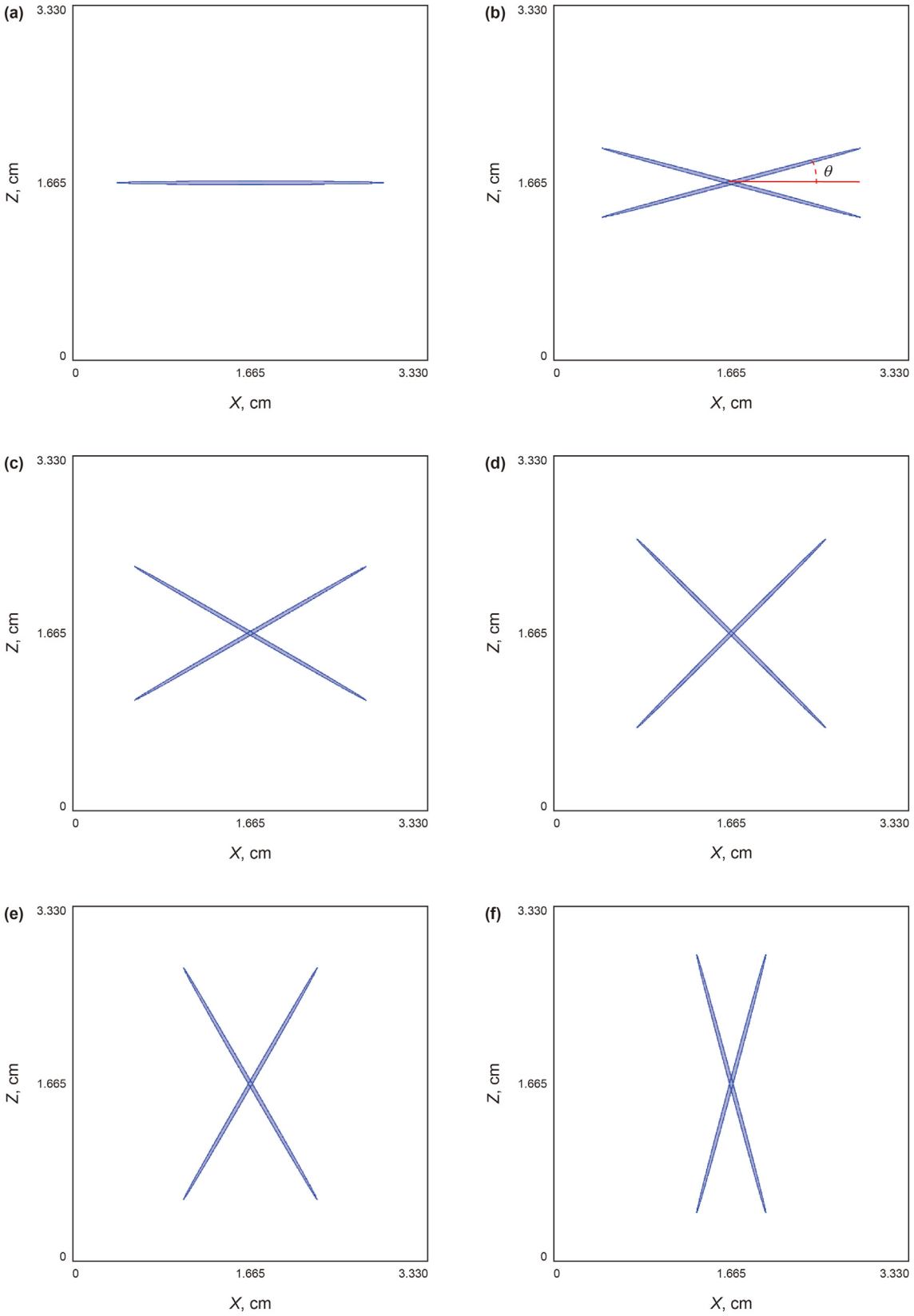

Fig. 11. Illustration of the synthetic rock samples with connected fractures designed to analyze the role of intersection angle between the fracture and the horizonal axis on attenuation and velocity dispersion. In addition, two fractures are exactly symmetrical with respect to the horizontal axis, and intersection angles of $\theta = 0^o$ (a), $\theta = 30^o$ (b), $\theta = 60^o$ (c), $\theta = 90^o$ (d), $\theta = 120^o$, (e) and $\theta = 150^o$ (f) are considered, respectively.

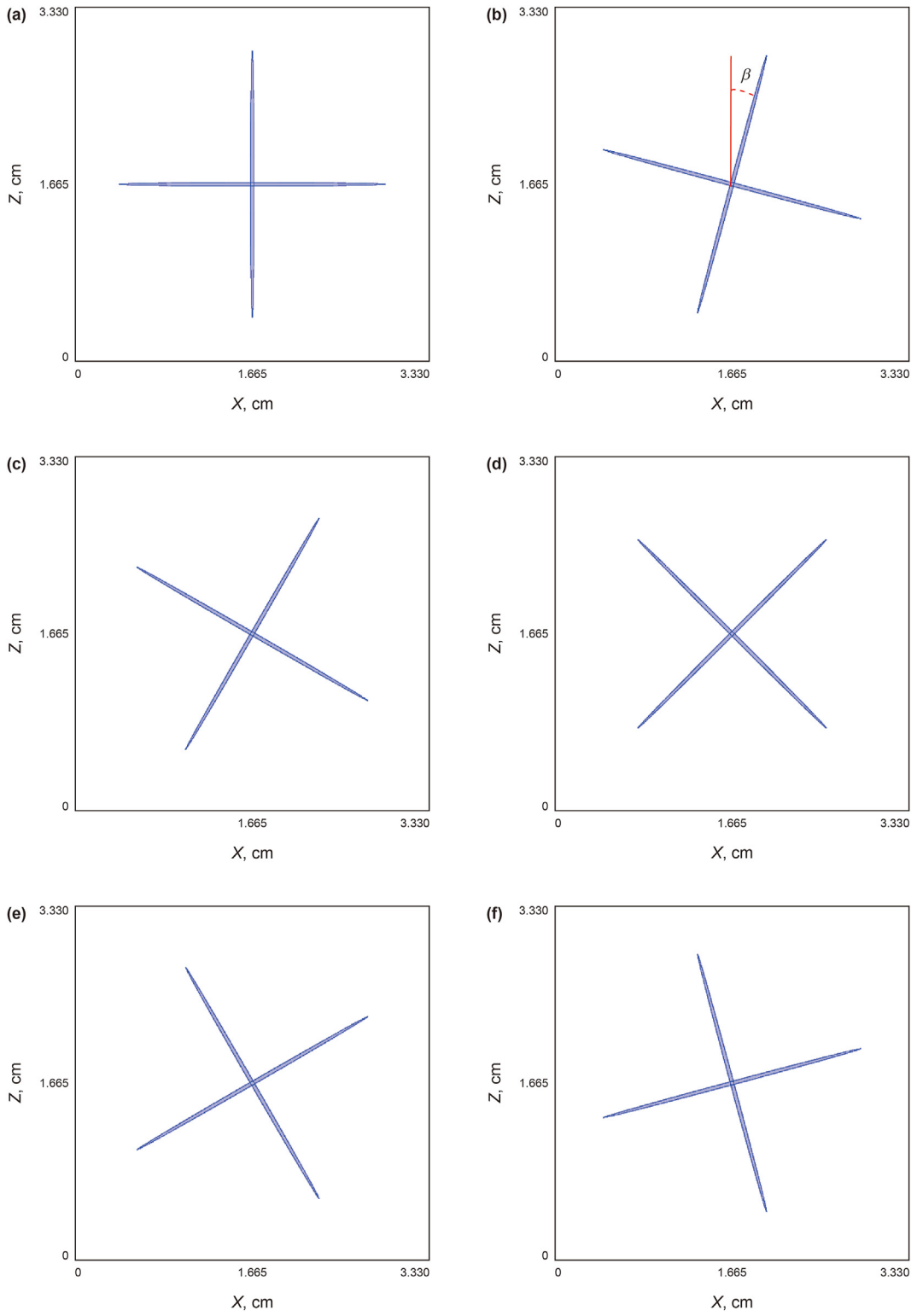

Fig. 12. Illustration of the synthetic rock samples with perpendicularly intersected fractures designed to analyze the role of P-wave propagating direction on attenuation and velocity dispersion. A series of intersection angles between the vertical axis and one of the fractures are considered, including $\beta = 0^o$ (a), $\beta = 15^o$ (b), $\beta = 30^o$ (c), $\beta = 45^o$ (d), $\beta = 60^o$ (e), and $\beta = 75^o$ (f).

peaks, it significantly affects the amplitudes of the second peak related to FF-WIFF, as shown in Fig. 13(e). We observe that the amplitude of the second attenuation peak is largest for $\beta = 0^o$ and is lowest for $\beta = 45^o$. In particular, the level of the second peak for $\beta = 15^o$ is equal to that for $\beta = 75^o$ and, correspondingly, the second peak magnitude for $\beta = 30^o$ is identical to that for $\beta = 60^o$. The magnitude of the first attenuation peak does not change regardless of varying intersection angle β, indicating that fluid flow between

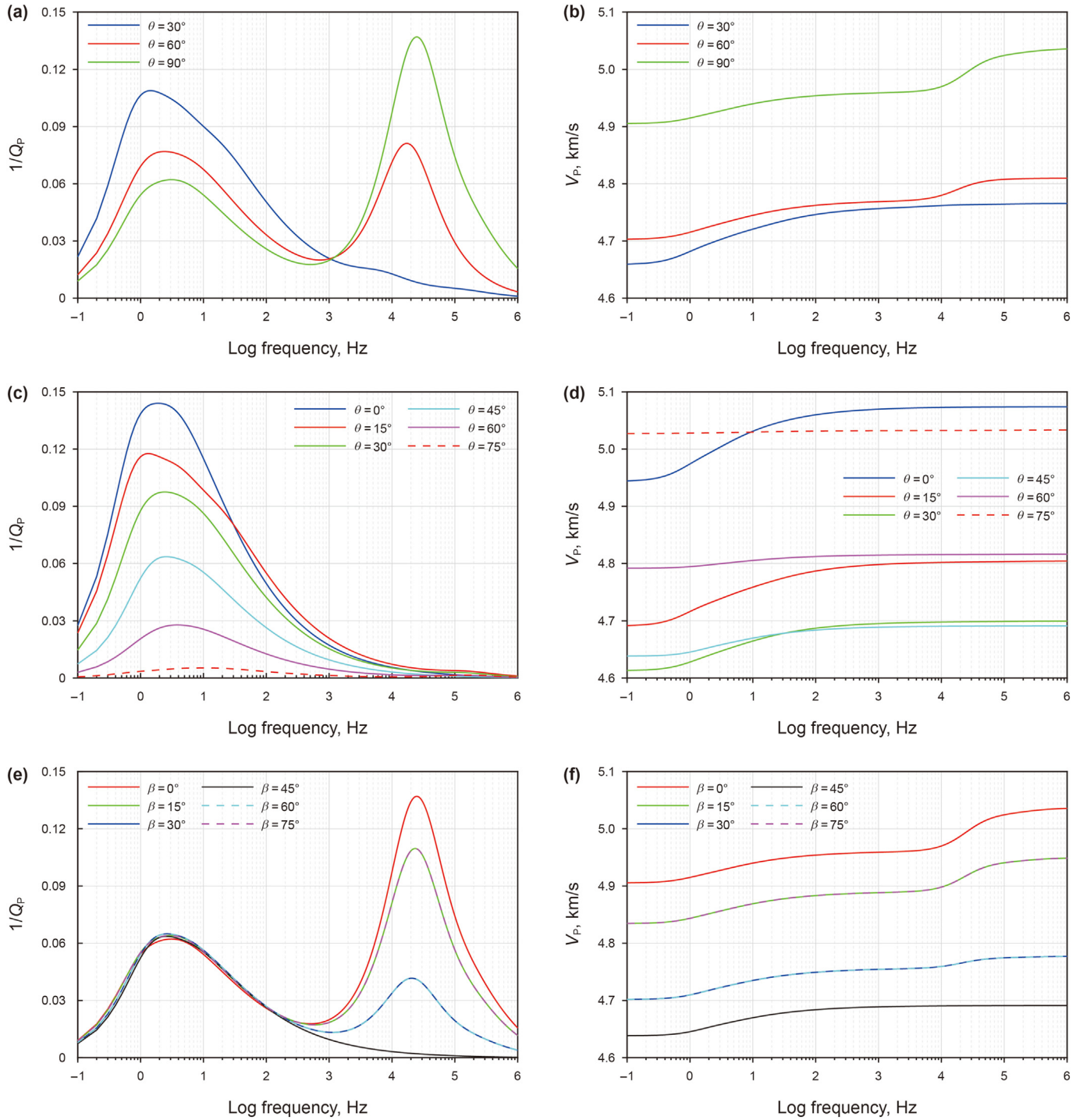

Fig. 13. Numerical results for inverse quality factor $1/Q_P$ (left column) and phase velocity V_P (right column) for vertically propagating P-wave as a function of frequency, obtained from the 2-D numerical quasi-static creep simulations of the poroelastic rock samples shown in Fig. 10 for (a and b), Fig. 11 (c and d) and Fig. 12 (e and f), respectively. Colored curves correspond to acoustic responses calculated for the fractured sample with various intersection angles, as indicated in the legend. The rock-frame and fluid properties are shown in Tables 1 and 2

the fractures and the background rocks are not affected for the rock sample with two perpendicularly intersected fractures. The corresponding phase velocity as a function of frequency (Fig. 13(f)) reveal a feather in agreement with the attenuation behavior and, this in turn indicates that phase velocity also encodes valuable information with regard to the fracture characters.

3.4. Effects of fracture infill on the stress interactions

To analyze the dependency between the behavior of attenuation and velocity dispersion due to WIFF and the fluid properties of the fractured porous rock sample, we first investigate the effects of fracture infills on dynamic stress interactions. We consider four different fluid saturation scenarios for the model in Fig. 3(b): the

background matrix saturated with brine and the intersected fractures saturated with three different fluids of brine, oil and supercritical CO_2 (i.e., $ScCO_2$); the background matrix saturated with oil and the intersected fractures saturated with the three different fluids; the background matrix saturated with $ScCO_2$ and the intersected fractures saturated with the three different fluids; the background matrix and the intersected fractures saturated with the same fluid. The resulting inverse quality factor and the corresponding phase velocity of P-wave as functions of frequency are displayed in Fig. 14.

It is important to notice that, while the pore fluid of the background rocks does not change apparently the characteristic transition frequency of the corresponding FB-WIFF attenuation peak for different fracture infills, it strongly affects the amplitude of the two attenuation peaks, as shown in Fig. 14(a), (c) and (e). In particular, we find that regardless of the pore fluid within the background rocks, the location of the FF-WIFF attenuation peak does not shift evidently but results in small amplitude variations for different fracture infill scenarios considered. In all scenarios, nevertheless, two characteristic frequency of the attenuation peaks is smallest for oil-filled fractures (red curves) and increases as fluid viscosity η decreases. The magnitude of the two attenuation peaks is largest for the brine-filled fractures (blue curves), and is lowest for the $ScCO_2$-filled fractures (green curves).

By comparing the three curves in Fig. 14(g), we observe that when the synthetic rock model is filled respectively with brine, oil and $ScCO_2$, significant variations in the magnitude and location of two attenuation peaks happen. In addition, the fluid pressure gradient corresponding to the fluid saturations of the rock model yields significant changes in the phase velocity behavior, as illustrated in the right column of Fig. 14. In particular, the velocity is largest for the model with brine saturation and is smallest for the model with $ScCO_2$ saturation. We also find that the frequency band of the FF-WIFF where velocity dispersion is broadest for the oil saturation and is narrowest for the $ScCO_2$ saturation, is in accord with the attenuation characteristics, which demonstrates that attenuation and phase velocity contain valuable information regard to the fluid property of the fractures.

The viscosity of fluid η is a key parameter that controls the prevailing fluid mobility and thus, the transition frequency of the two attenuation peaks in the fractured model. To identify the corresponding information that may be contained in seismoacoustic signatures, we consider the samples shown in Fig. 3(b) and Fig. 6(a), corresponding to the intersected fractures of Fracture 2 and Fracture 3. Fracture and background matrix of two samples are saturated by glycerin at five different temperatures T of 20^o, 40^o, 60^o, 80^o, and 100^o, where the fluid viscosity η decreases as T increases. Fig. 15(a) and (c) illustrates the calculated inverse quality factor as functions of frequency for vertically propagating P-wave. As expected based on our previous analysis, we observe that both samples produce two attenuation peaks related to FB-WIFF and FF-WIFF, which exhibit distinct characteristic frequencies. While the location of the first attenuation peak and the magnitude of second attenuation peak do not change significantly, we see that the first attenuation peak is more significant for the rock sample depicted in Fig. 6(a) due to increased amount of fluid flow between the fractures and the background rocks. Moreover, the fluid viscosity seems to shift the two attenuation peaks to a higher frequency as T increases.

Results in Fig. 15(b) and (15d) indicate that the frequency-dependent phase velocity also encodes useful information about fluid viscosity of the fractured porous rocks. Corresponding to the attenuation behavior, we find that the transition of significant velocity dispersion shifts towards higher frequency as η decreases. Furthermore, the measurable dispersion of phase velocity within seismic frequencies may prevail relying on the fluid viscosity of fractured media. Please also note the no-flow limit velocity at frequencies larger than 10^6 Hz.

4. Stress interaction effects on seismic reflection signatures

As WIFF changes significantly the phase velocity and the associated attenuation of fractured fluid-saturated rocks based on our previous calculations, we illustrate in this study its relevance simulating the seismic energy spreading and exploring the seismic characteristics of the compressional waves associated with a designed surface-based seismic experiment, for a deep formation saturated with supercritical CO_2. We assume that $ScCO_2$ is reserved in a subsurface storage site with a perfect overburden seal and no CO_2 is escaped from the deeper reservoir. The geological sequence of a rounded anticline is at a depth of 2.5 km (i.e., ~50 MPa) and ~1.5 km in length, and consists of a sandstone basement covered by a shale layer which is about 500 m thick and 1.5 km in depth in the center of the considered region (Fig. 16(a)). Elastic properties for each lithology were adopted according to literature (e.g., Tisato and Quintal, 2013; Al-Zaidi et al., 2018). Two scenarios were investigated here, via assuming the connected fractures of the reservoir domain were filled either by brine (case i) or $ScCO_2$ (case ii), while the porous background medium was saturated with brine. Thus, this semielliptical area exhibits P-wave velocity dispersion and attenuation behaviors similar to that shown in Fig. 14(a) and (b). Please also note viscoelastic properties of the fractured porous reservoir saturated with brine containing $ScCO_2$ may not be similar to those predicted in Fig. 14.

The simulation of seismic responses in the 2-D model (Fig. 16(a)) was performed in the frequency domain using acoustic wave equation-based 9-point finite-difference algorithm (e.g., Jo et al., 1996), and the 2-D acoustic wave equation in viscoelastic media is expressed as

$$\frac{\partial^2 U(x,z,\omega)}{\partial x^2}+\frac{\partial^2 U(x,z,\omega)}{\partial z^2}-\frac{\omega^2}{V^2(x,z)}U(x,z,\omega)=-f(x,z,\omega), \tag{11}$$

here U denotes the pressure wavefield, ω represents the angular frequency, V represents the frequency-dependent, complex valued velocity, and f represents the source. In addition, the absorbing boundary conditions were employed on the top, bottom, left and right sides of the geologic model. An explosive source of Ricker wavelet with its central frequency of 30 Hz and above the sequence site (see the star in Fig. 16(a)) $[x, z] = [2000, 15]$ m was excited to generate compressional waves acting in all directions and seismic reflections are acquired by geophones on the surfaces.

The reflected waves recorded by five geophones located at $z = 15$ m and x between 1.0 and 2.0 km, as denoted in Fig. 16(a) are illustrated in Fig. 16(b). The snapshots showing the P-wave propagation at four consecutive times ($t = 0.25$, 0.5, 0.8 and 1.0 s) are displayed in Fig. 16(c). We observe that the reflected waves generated due to the fractured storage site region are quite observable. It is also very interesting to see that amplitudes of acquired traces for case (ii) were slightly smaller than those acquired in case (i) at near offsets, while the observed reflection amplitude for case (ii) shows a variation up to 43% compared to those in case (i) at the $x = 2000$ m offset. The observed anomalies in Fig. 16(b) and (c) imply that the variations in the fractured porous reservoir due to $ScCO_2$ injection can produce apparent perturbations on seismic reflection signatures, which can be affected by seismic attenuation and velocity dispersion as compressional waves propagate through the CO_2 sequestration reservoir.

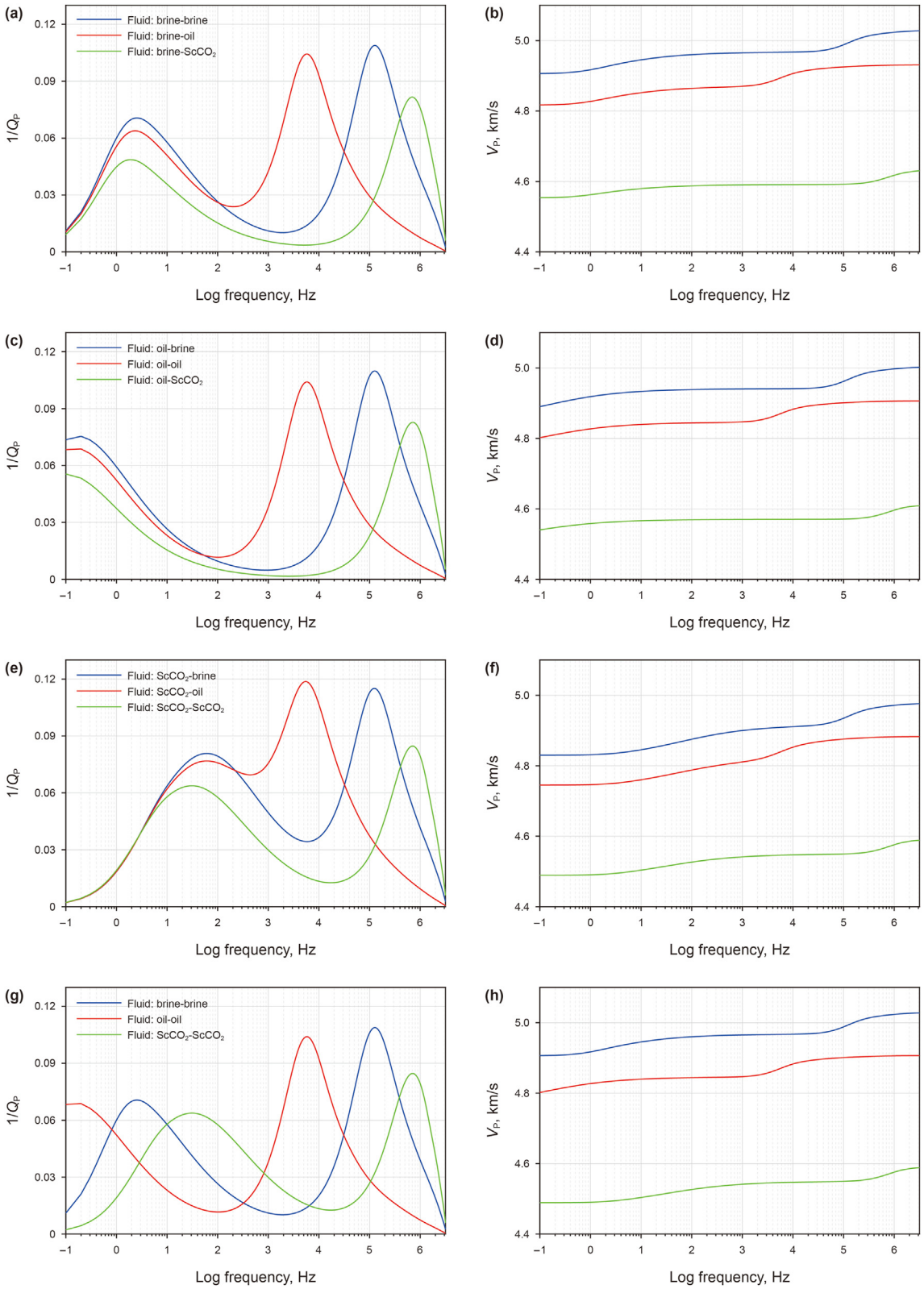

Fig. 14. Numerical results for inverse quality factor $1/Q_P$ (left column) and phase velocity V_P (right column) for the vertically propagating P-wave as a function of frequency, obtained for a numerical model consisting of two quasi-orthogonal mesoscopic intersected fractures shown in Fig. 3(b). The rock-frame and fluid properties are shown in Tables 1 and 2. Colored curves correspond to acoustic responses calculated for the fractured sample with various fracture infills. The legend terms refer to four fluid saturation scenarios: the background matrix saturated with brine and the connected fractures saturated with three different fluids (brine, oil and supercritical CO_2) (a and b); the background matrix saturated with oil and the connected fractures saturated with the three different fluids (c and d); the background matrix saturated with $ScCO_2$ and the connected fractures saturated with the three different fluids (e and f); the background matrix and the connected fractures saturated with the same fluid (g and h).

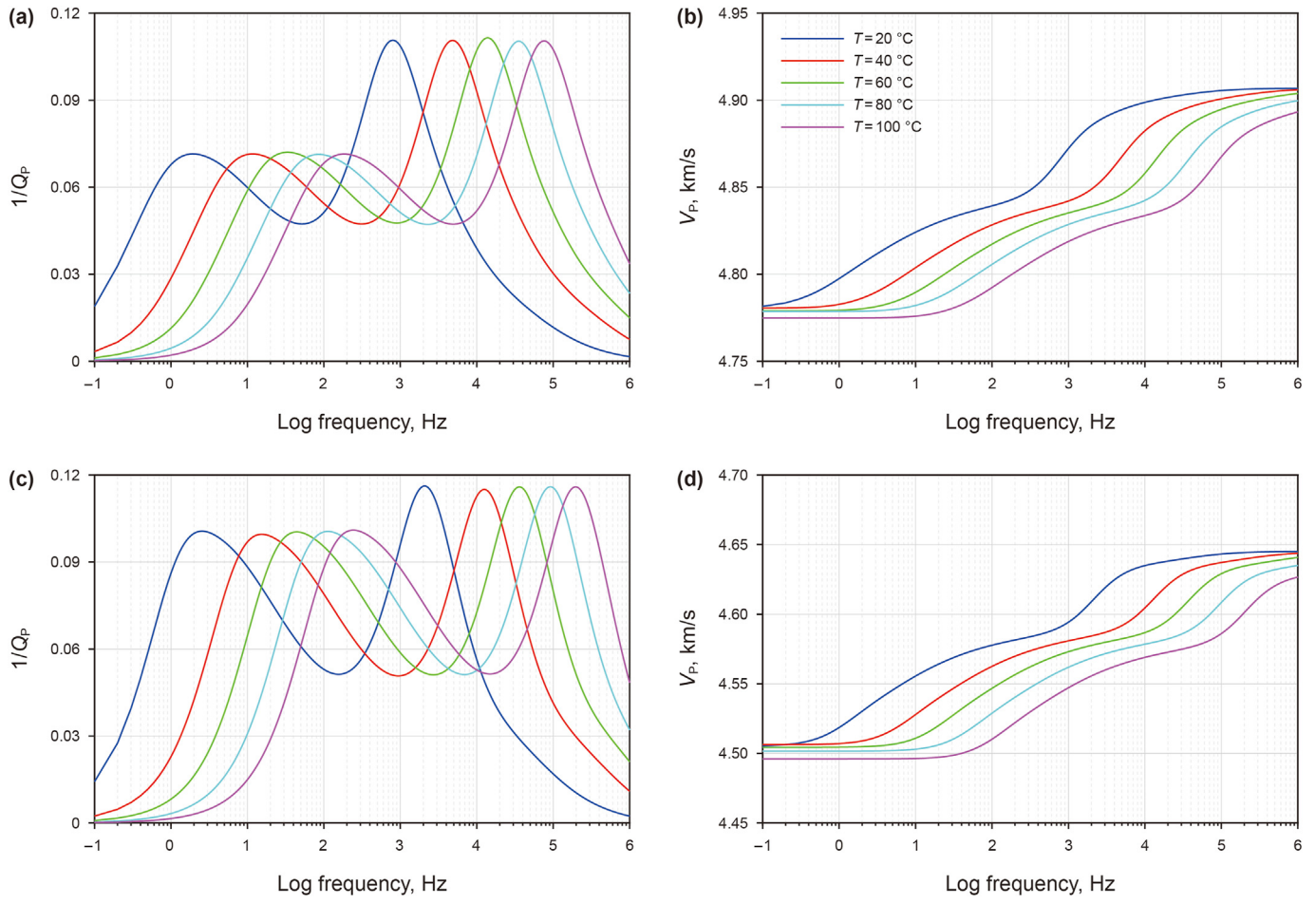

Fig. 15. Numerical results for inverse quality factor $1/Q_P$ (left column) and phase velocity V_P (right column) for vertically propagating P-wave as a function of frequency, obtained from the 2-D numerical quasi-static creep simulations for the poroelastic rock samples shown in Fig. 3(b) and Fig. 6(a), corresponding to the intersected fractures of Fracture 2 (a and b) and Fracture 3 (c and d). Colored curves correspond to the acoustic properties obtained under glycerin saturation at five different temperatures, as indicated in the legend, which correspond to various fluid viscosity. The rock-frame and fluid properties are shown in Tables 1 and 2. We observe that the two attenuation peaks, in association with FB- and FF-WIFF, exhibit two distinct characteristic frequencies for the fractured rock samples. Please notice the no-flow limit velocity at frequencies larger than 10^6 Hz.

5. Conclusions

Through a quasi-static finite element numerical upscaling procedure presented in this study, we investigated the effect of dynamic elastic interactions related to fracture connectivity on the WIFF characteristics between fractures and the background medium as well as within the connected fractures, and hence on the dynamic elastic properties of seismic waves in 2-D fractured fluid-saturated poroelastic rocks. On the basics of the finite element solution of the classical Biot's quasi-static poroelastic equations of consolidation (Biot, 1941) in the displacement-pressure formulation, which provides natural boundary conditions for no fluid flow and thus is consistent with an undrained rock sample, we performed numerical oscillatory compressibility relaxation experiments on a 2-D synthetic rock sample representative of the material containing either connected or unconnected mesoscopic fractures. The resulting complex-valued frequency-dependent equivalent compressional wave moduli obtained from the simulated stress-strain relations were employed to calculate frequency-dependent P-wave phase velocity and attenuation (or inverse quality factor) due to WIFF at the mesoscopic scale. Our results demonstrate that mesoscale fractures oriented quasi-perpendicular to the direction of wave propagation, in the unconnected scenario, results in significant seismic attenuation and velocity dispersion dominated by WIFF in the fractures and the embedding porous matrix. When the fractures are intersected, however, we observe that characteristics of P-wave attenuation and velocity dispersion change strongly. In particular, a slight reduction in the attenuation peak level corresponding to the unconnected fractures occurs, together with the presence of a second attenuation peak with high magnitude related to fluid flow through the communicating fractures, from one fracture into the other one. In addition, considering that the different effective permeabilities associated with the two dominant fluid flow paths lead to different frequency/time dependency of wave energy dissipation phenomena, the characteristic frequency related to intersected fractures is higher than the one related to the unconnected scenario. Our predictions also show that velocity dispersion, in the connected scenario, holds in a broader frequency region, and an apparent velocity decrease happens for several frequencies compared with the unconnected scenario. This phenomenon is due to the fact that, for lower frequencies or longer simulation times, fluid pressure was equilibrated very rapidly in the unconnected fractures compared with that in the connected scenario, as observed from the corresponding snapshots of the normalized fluid pressure state computed.

Since all fractured rock masses typically exhibit a varying degree of interconnectivity, the corresponding additional WIFF

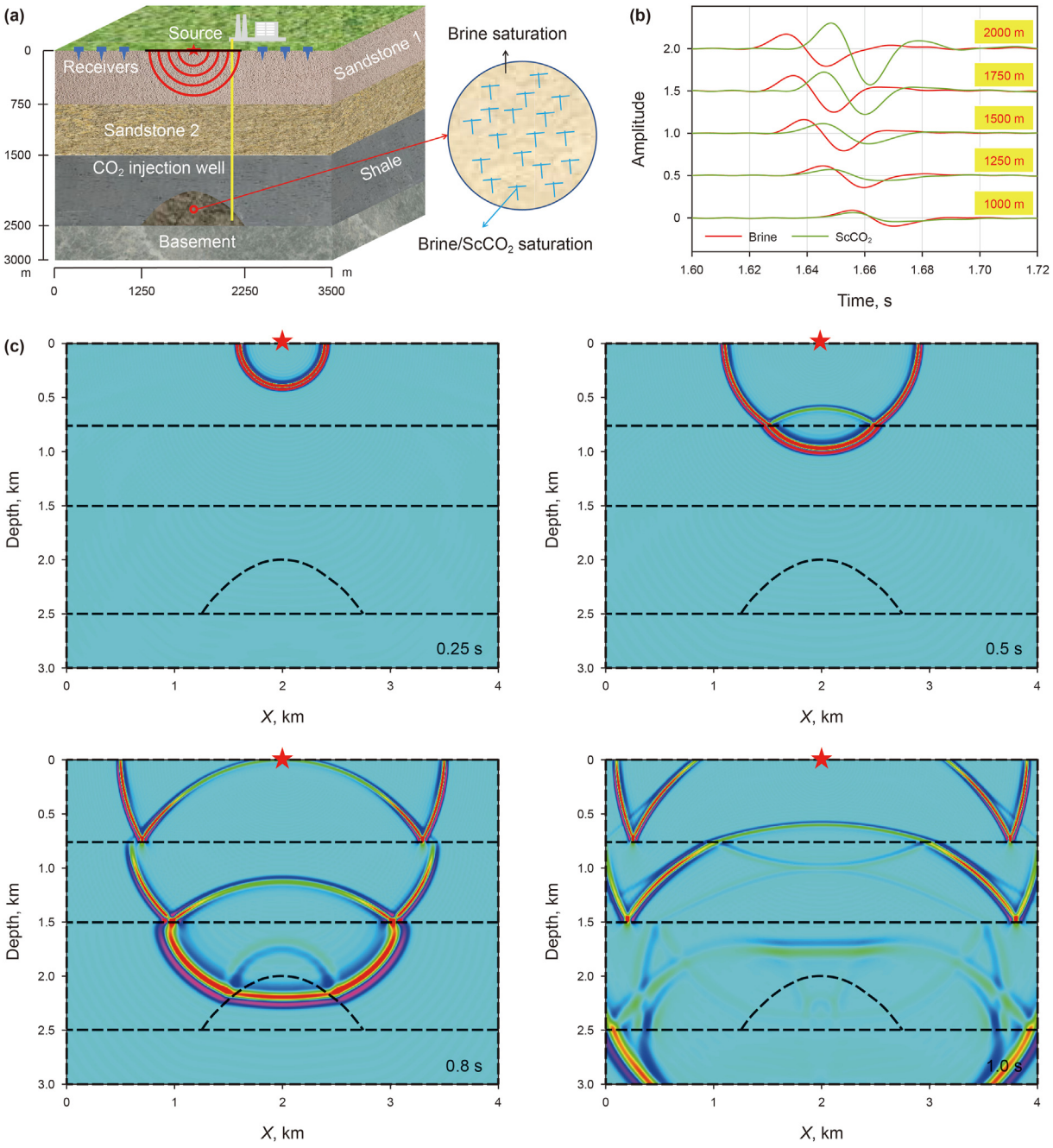

Fig. 16. The velocity dispersion and attenuation effects on the seismic responses of a geologic CO_2 storage site. (a) Illustration of supercritical CO_2 injection into a fractured porous reservoir which already contains brine. The thickness and sequence of geologic layers are also shown. (b) Seismic waves generated at the source point are recorded at five different offsets on the surface, in the cases of fractures filled with brine and ScCO2, respectively. Here, the reservoir exhibits P-wave velocity dispersion and attenuation similar to that shown in Fig. 14, and the observed reflection amplitude shows a variation up to 43% at the 2000 m offset. (c) The snapshots of wavefield for case (ii) indicate the compressional wave propagations at four successive times of 0.25, 0.5, 0.8 and 1.0 s, respectively.

contribution arising in the presence of intersected fractures should be considered in order to more practically examine seismic wave propagation behaviors with attenuation and velocity dispersion in such kinds of environments. A series of numerical simulations was performed to systematically analyze the role played by different characteristics of the connected fracture scenarios on the two amplifications of WIFF, as well as to explore the physical processes involved. The computed results demonstrate that velocity dispersion and the associated attenuation are sensitive to several key features of the fractured rocks, including connectivity, aperture and inclination of the fractures, as well as the fracture infills.

Moreover, in light of the fact that the combined effects of two amplified WIFF mechanisms contain valuable information about the hydraulic and mechanical characteristics of the probed fractured media, we believe that a deeper understanding of the associated fluid pressure diffusion processes taking place on a much smaller mesoscopic scale, via furthermore study on this topic by both numerical computations and laboratory measurements of

elastic properties at seismic frequency band, may eventually reveal interesting perspectives for more quantitative descriptions of fractured rocks and reservoir dynamic monitoring using seismic observations.

Acknowledgements

This work was supported financially by the NSFC Basic Research Program on Deep Petroleum Resource Accumulation and Key Engineering Technologies (U19B6003-04-03), Beijing Natural Science Foundation (8222073), the National Natural Science Foundation of China (41930425, 41804104), the Science Foundation of China University of Petroleum (Beijing) (2462020YXZZ008), the National Key Research and Development Program of China (2018YFA0702504), the Science Foundation of SINOPEC Key Laboratory of Geophysics (33550006-20-ZC0699-0001), and the Integration and Application of Deep Earth Exploration Data (DD20190435).

Appendix A. Displacement-Pressure Formulation of Quasi-static Poroelasticity of Biot's Consolidation Equations

The displacement-pressure ($u-p$) formulation of quasi-static poroelasticity of Biot's consolidation equations (Biot, 1941) in the space-time domain are given by

$$-(\nabla\cdot\boldsymbol{\sigma})=0, \tag{A1}$$

$$\nabla\cdot\left(-\frac{\kappa}{\eta}\nabla p\right)+\alpha\nabla\cdot\dot{\boldsymbol{u}}+\frac{\dot{p}}{M}=0, \tag{A2}$$

here a dot on the top of a variable represents the first partial time derivative, $\boldsymbol{\sigma}\equiv\sigma_{ij}$ represents the total stress tensor, the symbol ∇ represents the Nabla operator for spatial derivatives, p is the pore fluid pressure, and $\boldsymbol{u}$ is the solid displacements with components u_i in the ith direction (e.g., $i=[x,z]$ for the 2-D case). The ratio of the rock permeability κ and the viscosity of the pore fluid η denotes the hydraulic conductivity or fluid mobility (e.g., Batzle et al., 2006). $\alpha=1-K_d/K_s$ is the Biot-Willis coefficients, and $M=\left[(\alpha-\varphi)/K_s+\varphi/K_f\right]^{-1}$ is the fluid storage coefficient. φ is rock porosity, and K_d, K_s and K_f represent bulk moduli of the dry frame, the solid grains and the pore fluid, respectively. In the compression test, the stress function $S(t)$ in Equation (2) is applied at the top boundary of the REV in the $z-$ direction. The undrained boundaries were implemented in all of our numerical simulations to ensure zero fluid flow using the weak formulation of Biot's quasi-static poroelasticity. In addition, the boundary conditions for solid displacement $\boldsymbol{u}$ are defined as

$$\frac{\partial u}{\partial x}=0,$$

and

$$\frac{\partial u}{\partial z}=0. \tag{A3}$$

This indicates zero is attributed to the displacement in the $x-$ direction at both the left and right boundaries; as well, the displacement in the $z-$ direction is set to zero for the bottom boundary.

The components of the stress tensor, σ_{ij}, are defined as (Biot, 1941)

$$\sigma_{ij}=2\mu\varepsilon_{ij}+\lambda e\delta_{ij}-\alpha p\delta_{ij}, \tag{A4}$$

here δ_{ij} is the Kronecker delta, and μ is the shear modulus of the saturated rock which is identical to that of the dry frame and $\lambda=K_d-2\mu/3$ is Lamé parameter. The components ε_{ij} are written as

$$\varepsilon_{ij}=\frac{1}{2}\left(\frac{\partial u_i}{\partial x_j}+\frac{\partial u_j}{\partial x_i}\right), \tag{A5}$$

and the cubical dilatation, e, is represented using the trace of the strain tensor

$$e=\varepsilon_{11}+\varepsilon_{22}. \tag{A6}$$

Appendix B. The 2-D Finite Element Discretization Scheme

According to Biot's consolidation equations (Equations A1 and A2) and the associated boundary conditions for the 2-D numerical model (Equation (A3)), the weak displacement-pressure ($u-p$) formulations are given by (see Quintal et al., 2011 for more detailed descriptions)

$$\nabla\cdot\begin{bmatrix}-(\lambda+2\mu)\dfrac{\partial u_x}{\partial x}-\lambda\dfrac{\partial u_y}{\partial y}+\left(1-\dfrac{K_m}{K_s}\right)p\\ -\mu\left(\dfrac{\partial u_x}{\partial y}+\dfrac{\partial u_y}{\partial x}\right)\\ -\mu\left(\dfrac{\partial u_x}{\partial y}+\dfrac{\partial u_y}{\partial x}\right)\\ -(\lambda+2\mu)\dfrac{\partial u_y}{\partial y}-\lambda\dfrac{\partial u_x}{\partial x}+\left(1-\dfrac{K_m}{K_s}\right)p\end{bmatrix}=0$$

$$\nabla\cdot\begin{bmatrix}-\dfrac{\kappa}{\eta}\dfrac{\partial p}{\partial x}\\ -\dfrac{\kappa}{\eta}\dfrac{\partial p}{\partial y}\end{bmatrix}+\left(1-\frac{K_m}{K_s}\right)\left(\frac{\partial u_x}{\partial x\partial t}+\frac{\partial u_y}{\partial y\partial t}\right)+\frac{1}{M}\frac{\partial p}{\partial t}=0 \tag{B1}$$

Therefore, for finite element simulation via the solver COMSOL Multiphysics, the Biot's equations of consolidation in the $u-p$ formulation can be solved using the following partial differential equation

$$e_a\frac{\partial^2\boldsymbol{v}}{\partial t^2}+d_a\frac{\partial\boldsymbol{v}}{\partial t}+\nabla\cdot\Gamma=f, \tag{B2}$$

where e_a represents the mass coefficient, d_a represents the damping coefficient, Γ represents the conserved flux, and f represents the source. The four parameters are given, respectively, by

$$e_a=\begin{bmatrix}0&0&0\\0&0&0\\0&0&0\end{bmatrix}, \tag{B3}$$

$$d_a=\begin{bmatrix}0&0&0\\0&0&0\\0&0&\dfrac{1}{M}\end{bmatrix}, \tag{B4}$$

$$\Gamma = \begin{bmatrix} -(\lambda+2\mu)\dfrac{\partial u_x}{\partial x} - \lambda\dfrac{\partial u_y}{\partial y} + \left(1-\dfrac{K_m}{K_s}\right)p \\ -\mu\left(\dfrac{\partial u_x}{\partial y}+\dfrac{\partial u_y}{\partial x}\right) \\ -\mu\left(\dfrac{\partial u_x}{\partial y}+\dfrac{\partial u_y}{\partial x}\right) \\ -\dfrac{\kappa}{\eta}\dfrac{\partial p}{\partial x} \\ -\dfrac{\kappa}{\eta}\dfrac{\partial p}{\partial y} \end{bmatrix} \quad \begin{matrix} \\ -(\lambda+2\mu)\dfrac{\partial u_y}{\partial y} - \lambda\dfrac{\partial u_x}{\partial x} + \left(1-\dfrac{K_m}{K_s}\right)p \\ \\ \\ \end{matrix}, \tag{B5}$$

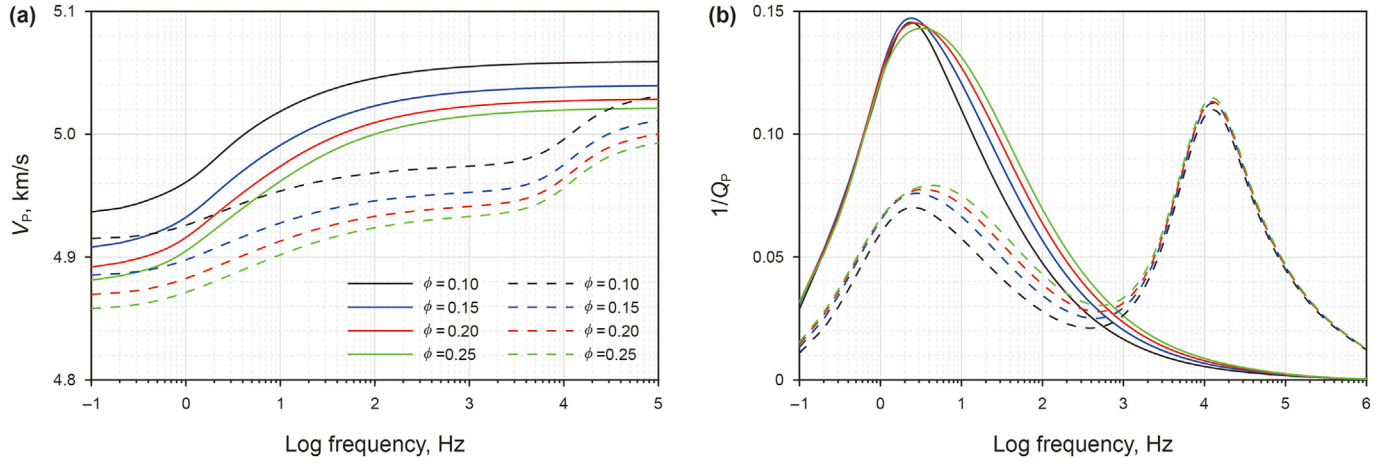

Fig. C1. Numerical results for phase velocity V_P (a) and inverse quality factor $1/Q_P$ (b) of vertically propagating P-wave as functions of frequency, for the poroelastic rock samples with unconnected (Fracture 1) and connected fractures (Fracture 2), respectively, as shown in Fig. 3. The rock-frame and fluid properties are shown in Tables 1 and 2. The solid lines represent attributes from the Fracture 1 and the dashed lines from the Fracture 2. Curves: black indicates background porosity $\varphi = 0.1$ (see Fig. 5), blue indicates $\varphi =$ 0.15, red indicates $\varphi = 0.2$, and green indicates $\varphi = 0.25$.

$$f = \begin{bmatrix} 0 \\ 0 \\ -\left(1-\dfrac{K_m}{K_s}\right)\left(\dfrac{\partial u_x}{\partial x \partial t}+\dfrac{\partial u_y}{\partial y \partial t}\right) \end{bmatrix}. \tag{B6}$$

In addition, for 2-D case, $\boldsymbol{v} = [v_x, v_y, p], \nabla = \left[\frac{\partial}{\partial x}, \frac{\partial}{\partial y}\right]$

Appendix C. The impact of background porosity φ on velocity dispersion and attenuation

For the considered poroelastic model embodying two fractures without and with hydraulic connectivity in Fig. 3, we investigate here the effect of matrix porosity φ on velocity dispersion and attenuation of P-wave. Figure C1 illustrates that an increase of φ produces a considerable decline in phase velocity across a wide frequency range. The variations in φ result in an observable perturbation on $1/Q_P$ within the frequency $10^{-1} - 10^3$ Hz, while the attenuation was barely impacted at higher frequency range for the rock sample with two intersected fractures. This is expected, because the changes in background porosity cause to the variations of compressibility contrast between the quasi-horizontal fracture and the background matrix, leading to an apparent perturbation of WIFF between the two materials corresponding to the imposed compressive stress.

References

Al-Zaidi, E., Fan, X.F., Edlmann, K., 2018. Supercritical CO_2 behaviour during water displacement in a sandstone core. Int. J. Greenh. Gas Control 79, 200–211. https://doi.org/10.1016/j.ijggc.2018.11.005.

Batzle, M.L., Han, D.H., Hofmann, R., 2006. Fluid mobility and frequency-dependent seismic velocity - direct measurements. Geophysics 71, N1–N9. https://doi.org/10.1190/1.2159053.

Biot, M., 1941. General theory of three-dimension consolidation. J. Appl. Phys. 12, 155–164. https://doi.org/10.1063/1.1712886.

Biot, M., 1956a. Theory of propagation of elastic waves in a fluid-saturated porous solid. I. Low-frequency range. J. Acoust. Soc. Am. 28, 168–178. https://doi.org/10.1121/1. 1908239.

Biot, M., 1956b. Theory of propagation of elastic waves in a fluid-saturated porous solid. II. Higher frequency range. J. Acoust. Soc. Am. 28, 179–191. https://doi.org/10.1121/1.1908241.

Cao, C.H., Fu, L.Y., Ba, J., Zhang, Y., 2019. Frequency- and incident-angle-dependent P-wave properties influenced by dynamic stress interactions in fractured porous media. Geophysics 84 (5), MR173–MR184. https://doi.org/10.1190/GEO2018-0103.1.

Caspari, E., Milani, M., Rubino, J.G., Müller, T.M., Quintal, B., Holliger, K., 2016. Numerical upscaling of frequency-dependent P- and S-wave moduli in fractured porous media. Geophys. Prospect. 64, 1166–1179. https://doi.org/10.1111/1365-2478.12393.

Caspari, E., Novikov, M., Lisitsa, V., Barbosa, N.D., Quintal, B., Rubino, J.G., Holliger, K., 2019. Attenuation mechanisms in fractured fluid-saturated porous rocks: a numerical modelling study. Geophys. Prospect. 67, 935–955. https://doi.org/10.1111/1365-2478.12667.

Chapman, M., Maultzsch, S., Liu, E., Li, X.-Y., 2003. The effect of fluid saturation in an anisotropic multi-scale equant porosity model. J. Appl. Geophys. 54, 191–202 https://doi.org/10.101/j.jappgeo.2003.01.003.

Galvin, R.J., Gurevich, B., 2015. Frequency-dependent anisotropy of porous rocks with aligned fractures. Geophys. Prospect. 63, 141–150. https://doi.org/10.1111/1365-2478.12177.

Grab, M., Quintal, B., Caspari, E., Deuber, C., Maurer, H., Greenhalgh, S., 2017. The effect of boiling on seismic properties of water-saturated fractured rock. J. Geophys. Res. 122, 9228–9252. https://doi.org/10.1002/2017JB014608.

Guo, J.X., Rubino, J.G., Barbosa, N.D., Glubokovskikh, S., Gurevich, B., 2018. Seismic dispersion and attenuation in saturated porous rocks with aligned fractures of finite thickness: theory and numerical simulations – Part 1: P-wave perpendicular to the fracture plane. Geophysics 83 (1), WA49–WA62. https://doi.org/10.1190/GEO2017-0065.1.

Gurevich, B., Brajanovski, M., Galvin, R., Müller, T.M., Toms-Stewart, J., 2009. P-wave dispersion and attenuation in fractured and porous reservoir – poroelasticity approach. Geophys. Prospect. 57, 225–237. https://doi.org/10.1111/j.1365-2478.2009.00785.x.

He, Y.X., Li, X.L., Tang, G.Y., Dong, C.H., Chen, M., Wang, S.X., 2021. Modeling the effects of fracture infill on frequency-dependent anisotropy and AVO response of a fractured porous layer. Petrol. Sci. 18, 758–772. https://doi.org/10.1007/s12182-021-00555-0.

He, Y.-X., Wang, S.X., Sun, C., Tang, G.Y., Zhu, W., 2021. Analysis of the frequency dependence characteristics of wave attenuation and velocity dispersion using a poroelastic model with mesoscopic and miceoscopic heterogeneities. Geophys. Prospect. 69, 2160–2181. https://doi.org/10.1111/1365-2478.13101.

He, Y.-X., Wang, S.X., Wu, X.Y., Xi, B., 2020. Influence of frequency-dependent anisotropy on seismic amplitude-versus-offset signatures for fractured poroelastic media. Geophys. Prospect. 68, 2141–2163 https://doi.org/10.111171365-2478.12981.

Jo, C.H., Shin, C.S., Suh, J.H., 1996. An optimal 9-point, finite-difference, frequency-space, 2-D scalar wave extrapolator. Geophysics 61, 529–537. https://doi.org/10.1190/1.1443979.

Kong, L.Y., Gurevich, B., Müller, T.M., Wang, Y.B., Yang, H.Z., 2013. Effect of fracture fill on attenuation and dispersion in fractured rocks. Geophys. J. Int. 195, 1679–1688. https://doi.org/10.1093/gji/ggt354.

Krief, M., Garat, J., Stellingwerff, J., Ventre, J., 1990. A petrophysical interpretation using the velocities of P and S waves (full waveform inversion). Log. Anal. 31, 355–369.

Lissa, S., Barbosa, N., Rubino, J.G., Quintal, B., 2019. Seismic attenuation and dispersion in poroelastic media with fractures of variable aperture distributions. Solid Earth 10, 1321–1336. https://doi.org/10.5194/se-10-1321-2019.

Masson, Y.J., Pride, S.R., 2007. Poroelastic finite-different modeling of seismic attenuation and dispersion due to mesoscopic-scale heterogeneity. J. Geophys. Res. 112, B03204. https://doi.org/10.1029/2006JB004592.

Maultzsch, S., Chapman, M., Liu, E.R., Li, X.Y., 2003. Modelling frequency-dependent seismic anisotropy in fluid-saturated rock with aligned fractures: implication of fracture size estimation from anisotropic measurements. Geophys. Prospect. 51, 381–392. https://doi.org/10.1046/j.1365-2478. 2003.00386.x.

Mavko, G., Mukerji, T., Dvorkin, J., 2009. The Rock Physics Handbook: Tools for Seismic Analysis of Porous Media, second ed. Cambridge Univ. Press, Cambridge.

Mikhaltsevitch, V., Lebedev, M., Gurevich, B., 2016. Validation of the laboratory measurement at seismic frequencies using the Kramers-Kronig relationship. Geophys. Res. Lett. 43, 4986–4991. https://doi.org/10.1002/2016GRL069269.

Müller, T.M., Gurevich, B., Lebedev, M., 2010. Seismic wave attenuation and dispersion resulting from wave-induced flow in porous rocks– A review. Geophysics 75, 147–164. https://doi.org/10.1190/1.3463417.

Nakagawa, S., Schoenberg, M.A., 2007. Poroelastic modelling of seismic boundary conditions across a fracture. J. Acoust. Soc. Am. 122, 831–847. https://doi.org/10.1121/1.2747206.

Pang, S., Stovas, A., Xing, H.L., 2021. Frequency-dependent anisotropy in partially saturated porous rock with multiple sets of mesoscale fractures. Geophys. J. Int. 227, 147–161. https://doi.org/10.1093/gji/ggab204.

Quintal, B., Steeb, S., Frehner, M., Schmalholz, S.M., 2011. Quasi-static finite element modeling of seismic attenuation and dispersion due to wave-induced fluid flow in poroelastic media. J. Geophys. Res. 116, B1201. https://doi.org/10.1029/2010JB007475.

Quintal, B., Janicke, R., Rubino, J.G., Steeb, S., Holliger, K., 2014. Sensitivity of S-wave attenuation to the connectivity of fractures in fluid-saturated rocks. Geophysics 79, WB15–WB24. https://doi.org/10.1190/GEO2013-0409.1.

Rubino, J.G., Caspari, E., Müller, T.M., Milani, M., Barbosa, N., Holliger, K., 2016. Numerical upscaling in 2D heterogeneous poroelastic rocks. J. Geophys. Res. 121, 6698–6721. https://doi.org/10.1002/2016JB13165.

Rubino, J.G., Guarracino, E., Müller, T.M., Holliger, K., 2013a. Do seismic waves sense fracture connectivity? Geophys. Res. Lett. 40, 692–696. https://doi.org/10.1002/grl.50127.

Rubino, J.G., Monachesi, L.B., Müller, T.M., Guarracino, L., Holliger, K., 2013b. Seismic wave attenuation and dispersion due to wave-induced fluid flow with strong permeability fluctuations. J. Acoust. Soc. Am. 134, 4742–4751. https://doi.org/10.1121/1.4824967.

Rubino, J.G., Müller, T.M., Guarracino, L., Milani, M., Holliger, K., 2014. Seismoacoustic signatures of fracture connectivity. J. Geophys. Res. Solid Earth 119, 2252–2271. https://doi.org/10.1002/2013JB10567.

Rubino, J.G., Ravazzoli, C.L., Santos, J., 2009. Equivalent viscoelastic solids for heterogeneous fluid-saturated porous rocks. Geophysics 74 (1), N1–N13. https://doi.org/10.1190/1.3008544.

Solazzi, S.G., Guarracino, L., Rubono, J.G., Müller, T.M., Holliger, K., 2017. Modeling forced imbibition processes and the associated seismic attenuation in heterogeneous porous rocks. J. Geophys. Res. 122, 9031–9049. https://doi.org/10.1002/2017JB014636.

Tisato, N., Quintal, B., 2013. Measurements of seismic attenuation and transient fluid pressure in partially saturated Berea sandstone: evidence of fluid flow on the mesoscopic scale. Geophys. J. Int. 195, 342–351. https://doi.org/10.1093/gji/ggt259.

Wang, Y., Zhang, L.W., Soong, Y., Dilmore, R., Liu, H., Lei, H., Li, X.C., 2019. From core-scale experiment to reservoir reservoir-scale modeling: a scale-up approach to investigate reaction-induced permeability evolution of CO_2 storage reservoir and caprock at a U.S. CO_2 storage site. Comput. Geosci. 125, 55–68. https://doi.org/10.1016/j.cageo.2019.01.006.

Wenzlau, F., Altmann, J.B., Müller, T.M., 2010. Anisotropic dispersion and attenuation due to wave-induced flow: quasi-static finite-element modeling in poroelastic media. J. Geophys. Res. 115, B07204. https://doi.org/10.1029/2009JB006644.

Yin, H.J., Zhao, J.G., Tang, G.Y., Zhao, L.M., Ma, X.Y., Wang, S.X., 2017. Pressure and fluid effect on frequency-dependent elastic moduli in fully saturated tight sandstone. J. Geophys. Res. 122 (11), 8925–8942. https://doi.org/10.1002/2017JB014244.

Zhao, L.X., Yao, Q.L., Han, D.H., Yan, F., Nasser, M., 2016. Characterizing the effect of elastic interactions on the effective elastic properties of porous, cracked rocks. Geophys. Prospect. 64, 157–169. https://doi.org/10.1111/1365-2478.12243.

Zheng, L.Z., Wang, L.C., Deng, W., 2018. Seismicity enhances macrodispersion in finite porous and fractured domains: a pore-scale perspective. J. Geophys. Res. 124, 2844–2857. https://doi.org/10.1029/2018JB016921.